Title
Target Selection and Validation of DESI Quasars

Journal
The Astrophysical Journal, 944(1)

ISSN
0004-637X

Authors
Chaussidon, Edmond
Yèche, Christophe
Palanque-Delabrouille, Nathalie
et al.

Publication Date
2023-02-01

DOI
10.3847/1538-4357/acb3c2

The Astrophysical Journal, 944:107 (17pp), 2023 February 10 https://doi.org/10.3847/1538-4357/acb3c2

Target Selection and Validation of DESI Quasars

Edmond Chaussidon[1], Christophe Yèche[1], Nathalie Palanque-Delabrouille[1,2], David M. Alexander[3,4], Jinyi Yang[5], Steven Ahlen[6], Stephen Bailey[2], David Brooks[7], Zheng Cai[8], Solène Chabanier[2], Tamara M. Davis[9], Kyle Dawson[10], Axel de laMacorra[11], Arjun Dey[12], Biprateep Dey[13], Sarah Eftekharzadeh[14], Daniel J. Eisenstein[15], Kevin Fanning[16,17], Andreu Font-Ribera[18], Enrique Gaztañaga[19,20], Satya Gontcho A Gontcho[2], Alma X. Gonzalez-Morales[21,22], Julien Guy[2], Hiram K. Herrera-Alcantar[22], Klaus Honscheid[16,23], Mustapha Ishak[24], Linhua Jiang[25], Stephanie Juneau[12], Robert Kehoe[26], Theodore Kisner[2], Andras Kovács[27,28], Anthony Kremin[2], Ting-Wen Lan[29], Martin Landriau[2], Laurent Le Guillou[30], Michael E. Levi[2], Christophe Magneville[1], Paul Martini[16,17], Aaron M. Meisner[12], John Moustakas[31], Andrea Muñoz-Gutiérrez[11], Adam D. Myers[32], Jeffrey A. Newman[13], Jundan Nie[33], Will J. Percival[34,35,36], Claire Poppett[2,37,38], Francisco Prada[39], Anand Raichoor[2], Corentin Ravoux[1], Ashley J. Ross[16,17], Edward Schlafly[40], David Schlegel[2], Ting Tan[30], Gregory Tarlé[41], Rongpu Zhou[2], Zhimin Zhou[33], and Hu Zou[33]

[1] IRFU, CEA, Université Paris-Saclay, F-91191 Gif-sur-Yvette, France; christophe.yeche@cea.fr
[2] Lawrence Berkeley National Laboratory, 1 Cyclotron Road, Berkeley, CA 94720, USA
[3] Centre for Extragalactic Astronomy, Department of Physics, Durham University, South Road, Durham, DH1 3LE, UK
[4] Institute for Computational Cosmology, Department of Physics, Durham University, South Road, Durham DH1 3LE, UK
[5] Steward Observatory, University of Arizona, 933 N. Cherry Avenue, Tucson, AZ 85721, USA
[6] Physics Department, Boston University, 590 Commonwealth Avenue, Boston, MA 02215, USA
[7] Department of Physics & Astronomy, University College London, Gower Street, London, WC1E 6BT, UK
[8] Department of Astronomy, Tsinghua University, Beijing 100084, People's Republic of China
[9] School of Mathematics and Physics, University of Queensland, Brisbane, QLD, 4072, Australia
[10] Department of Physics and Astronomy, The University of Utah, 115 South 1400 East, Salt Lake City, UT 84112, USA
[11] Instituto de Física, Universidad Nacional Autónoma de México, Ciudad de México C.P. 04510, México
[12] NSF's NOIRLab, 950 N. Cherry Avenue, Tucson, AZ 85719, USA
[13] Department of Physics & Astronomy and Pittsburgh Particle Physics, Astrophysics, and Cosmology Center (PITT PACC), University of Pittsburgh, 3941 O'Hara Street, Pittsburgh, PA 15260, USA
[14] Universities Space Research Association, NASA Ames Research Center, Moffett Field, CA, USA
[15] Center for Astrophysics | Harvard & Smithsonian, 60 Garden Street, Cambridge, MA 02138, USA
[16] Center for Cosmology and AstroParticle Physics, The Ohio State University, 191 West Woodruff Avenue, Columbus, OH 43210, USA
[17] Department of Astronomy, The Ohio State University, 4055 McPherson Laboratory, 140 W 18th Avenue, Columbus, OH 43210, USA
[18] Institut de Física d'Altes Energies (IFAE), The Barcelona Institute of Science and Technology, Campus UAB, E-08193 Bellaterra Barcelona, Spain
[19] Institut d'Estudis Espacials de Catalunya (IEEC), E-08034 Barcelona, Spain
[20] Institute of Space Sciences, ICE-CSIC, Campus UAB, Carrer de Can Magrans s/n, E-08913 Bellaterra, Barcelona, Spain
[21] Consejo Nacional de Ciencia y Tecnología, Avenida Insurgentes Sur 1582. Colonia Crédito Constructor, Del. Benito Juárez C.P. 03940, México D.F. México
[22] Departamento de Física, Universidad de Guanajuato—DCI, C.P. 37150, Leon, Guanajuato, México
[23] Department of Physics, The Ohio State University, 191 West Woodruff Avenue, Columbus, OH 43210, USA
[24] Department of Physics, The University of Texas at Dallas, Richardson, TX, 75080, USA
[25] Kavli Institute for Astronomy and Astrophysics at Peking University, PKU, 5 Yiheyuan Road, Haidian District, Beijing 100871, People's Republic of China
[26] Department of Physics, Southern Methodist University, 3215 Daniel Avenue, Dallas, TX 75275, USA
[27] Departamento de Astrofísica, Universidad de La Laguna (ULL), E-38206, La Laguna, Tenerife, Spain
[28] Instituto de Astrofísica de Canarias, C/ Vía Láctea, s/n, E-38205 San Cristóbal de La Laguna, Santa Cruz de Tenerife, Spain
[29] Graduate Institute of Astrophysics and Department of Physics, National Taiwan University, No. 1, Sec. 4, Roosevelt Road, Taipei 10617, Taiwan
[30] Sorbonne Université, CNRS/IN2P3, Laboratoire de Physique Nucléaire et de Hautes Energies (LPNHE), F-75005 Paris, France
[31] Department of Physics and Astronomy, Siena College, 515 Loudon Road, Loudonville, NY 12211, USA
[32] Department of Physics & Astronomy, University of Wyoming, 1000 E. University, Department 3905, Laramie, WY 82071, USA
[33] National Astronomical Observatories, Chinese Academy of Sciences, A20 Datun Road, Chaoyang District, Beijing, 100012, People's Republic of China
[34] Department of Physics and Astronomy, University of Waterloo, 200 University Avenue W, Waterloo, ON N2L 3G1, Canada
[35] Perimeter Institute for Theoretical Physics, 31 Caroline Street North, Waterloo, ON N2L 2Y5, Canada
[36] Waterloo Centre for Astrophysics, University of Waterloo, 200 University Avenue West, Waterloo, ON N2L 3G1, Canada
[37] Space Sciences Laboratory, University of California, Berkeley, 7 Gauss Way, Berkeley, CA 94720, USA
[38] University of California, Berkeley, 110 Sproul Hall #5800, Berkeley, CA 94720, USA
[39] Instituto de Astrofisica de Andalucía, Glorieta de la Astronomía, s/n, E-18008 Granada, Spain
[40] Lawrence Livermore National Laboratory, P.O. Box 808 L-211, Livermore, CA 94551, USA
[41] University of Michigan, Ann Arbor, MI 48109, USA

Received 2022 August 22; revised 2022 November 23; accepted 2022 December 3; published 2023 February 28

Abstract

The Dark Energy Spectroscopic Instrument (DESI) survey will measure large-scale structures using quasars as direct tracers of dark matter in the redshift range $0.9 < z < 2.1$ and using Lyα forests in quasar spectra at $z > 2.1$. We present several methods to select candidate quasars for DESI, using input photometric imaging in three optical bands (g, r, z) from the DESI Legacy Imaging Surveys and two infrared bands (W1, W2) from the Wide-field

Infrared Survey Explorer. These methods were extensively tested during the Survey Validation of DESI. In this paper, we report on the results obtained with the different methods and present the selection we optimized for the DESI main survey. The final quasar target selection is based on a random forest algorithm and selects quasars in the magnitude range of $16.5 < r < 23$. Visual selection of ultra-deep observations indicates that the main selection consists of 71% quasars, 16% galaxies, 6% stars, and 7% inconclusive spectra. Using the spectra based on this selection, we build an automated quasar catalog that achieves a fraction of true QSOs higher than 99% for a nominal effective exposure time of ∼1000 s. With a 310 deg^{-2} target density, the main selection allows DESI to select more than 200 deg^{-2} quasars (including 60 deg^{-2} quasars with $z > 2.1$), exceeding the project requirements by 20%. The redshift distribution of the selected quasars is in excellent agreement with quasar luminosity function predictions.

Unified Astronomy Thesaurus concepts: Quasars (1319); Redshift surveys (1378); Sky surveys (1464)

1. Introduction

The Dark Energy Spectroscopic Instrument (DESI; Levi et al. 2013; DESI Collaboration et al. 2016a, 2016b; Abareshi et al. 2022) survey will measure with high precision the baryon acoustic feature imprinted on the large-scale structure of the universe, as well as the distortions of galaxy clustering due to redshift-space effects. To achieve these goals, the survey will make spectroscopic observations of four distinct classes of extragalactic sources—nearby bright galaxies (Ruiz-Macias et al. 2020), luminous red galaxies (Zhou et al. 2020), star-forming emission line galaxies (Raichoor et al. 2020), and quasars (Yèche et al. 2020). The survey will additionally include observations of Milky Way stars (Allende Prieto et al. 2020) to study the early assembly of the Milky Way Galaxy and perform flux calibration of all of the measurements.

In the past two decades, quasars (a.k.a. quasi-stellar objects, or QSOs) have become a key ingredient in our understanding of cosmology and galaxy evolution. Being among the most luminous extragalactic sources, they have become a mainstay of cosmological surveys such as the 2dF Quasar Redshift Survey (Croom et al. 2001) and the Sloan Digital Sky Survey (SDSS; York et al. 2000), where they are the source of choice to study large-scale structures at high redshift.

As part of the third generation of the Sloan Digital Sky Survey (SDSS-III; Eisenstein et al. 2011), the Baryon Acoustic Oscillation Survey (BOSS; Dawson et al. 2013) measured the spectrum of about 300,000 quasars, 180,000 of which are at $z > 2.15$, to a limiting magnitude of $g \sim 22$. As part of SDSS-IV, the extended Baryon Oscillation Spectroscopic Survey (eBOSS; Dawson et al. 2016) has observed 350,000 quasars with redshifts of $0.8 < z < 2.2$ to $g \sim 22.5$, in addition to targeting 60,000 new quasars at $z > 2.2$ (Lyke et al. 2020). DESI is aiming to quadruple the number of known quasars and to obtain spectra of nearly 3 million quasars, reaching limiting magnitudes of $r \sim 23$.

One can measure large-scale structures using QSOs as direct tracers of dark matter, and DESI will do so in the redshift range $0.9 < z < 2.1$. Spectroscopy of QSOs provides a precise, three-dimensional map of matter in the universe in which the scale of baryon acoustic oscillations can be measured at high precision. This spectroscopic sample of QSOs can also be used to probe the growth of structure through redshift-space distortions. This new field of research with quasars was pioneered by eBOSS (Zarrouk et al. 2018; Neveux et al. 2020; Alam et al. 2021; Hou et al. 2021).

At higher redshifts, one can utilize the foreground neutral-hydrogen absorption systems that make up the Lyα forest; DESI spectra cover the Lyα transition at $\lambda = 1216$ Å for objects at $z > 2.1$ (thereafter Lyα QSOs). At such redshift, the Lyα QSOs exhibit a significant amount of Lyα forest in their spectra in DESI. This field of research has developed over more than two decades (McDonald 2003; Busca et al. 2013; Slosar et al. 2013) and reached its peak with the two recent publications of eBOSS (Chabanier et al. 2019; du Mas des Bourboux et al. 2020).

QSOs are fueled by gravitational accretion onto super-massive black holes at the centers of these galaxies. The QSO emission can outshine that of the host galaxy by a large factor. Even in the nearest QSOs, the emitting regions are too small to be resolved, so QSOs will generally appear as point sources in images. QSOs are the brightest population of astrophysical targets with useful target density at redshifts $z > 1$ where the population peaks (Palanque-Delabrouille et al. 2016).

Because of their point-like morphology and photometric characteristics that mimic faint blue stars in optical wavelengths, especially for the Lyα QSOs, the QSO selection is challenging. Successful selection of a highly complete and pure QSO sample is usually based on their UV excess (Richards et al. 2002; Ross et al. 2012). In DESI we propose an alternative approach that detects their near-infrared (NIR) excess as already demonstrated in eBOSS (Myers et al. 2015). Indeed, we use three optical bands (g, r, z) combined with Wide-field Infrared Survey Explorer (WISE) infrared photometry in the W1 and W2 bands to select our primary sample of QSOs. QSOs are ∼2 mag brighter in the NIR at all redshifts compared to stars of similar optical magnitude and color, providing a powerful method for discriminating against contaminating stars.

In order to test the different target selection approaches and to optimize the exposure time for each target class before beginning 5 yr of DESI operations (hereafter main survey), DESI has performed a Survey Validation (SV), organized in two phases with separate goals.

The first phase of SV, completed in 4 months, allowed us to optimize the selection algorithms, estimate the redshift distributions, and evaluate the projected cosmology constraints. It provided spectra over 45 fields containing a mix of luminous red galaxy targets, emission line galaxy targets, and quasar targets. Among them, 42 fields have a total effective exposure time of $T_{\rm eff} \sim 4000$ s and three fields correspond to ultra-deep observations ($T_{\rm eff} \sim 10{,}000$ s). The latter observations have been visually inspected and those three fields provide a control sample to study the target selection.

The second stage, the 1% survey consisted of a full clustering program covering about 1% of the DESI survey with fiber assignments similar to the main survey and exposure times ∼30% longer than the nominal exposure time ($T_{\rm eff} \sim 1000$ s) projected for the main survey. It lasted

approximately 1 month. During the second phase of SV, we used the final quasar selection (hereafter "main selection"), which was optimized during the first phase of SV.

This paper is one of a suite of eight papers detailing targeting for DESI. Myers et al. (2022) presents all the documentation describing the target selection pipeline. The Lan et al. (2023) and Alexander et al. (2022) papers describe the construction of spectroscopic truth tables based on visual inspection for the galaxies and the QSO targets, respectively.

The selection of Milky Way stars, the nearby bright galaxies, luminous red galaxies, and emission line galaxies are presented in Cooper et al. (2022), Hahn et al. (2022), Zhou et al. (2022), and Raichoor et al. (2022), respectively. Finally, the quasar sample is presented in this paper. Those five target selection papers describe the DESI final samples, and supersede the preliminary target selections presented in Allende Prieto et al. (2020), Ruiz-Macias et al. (2020), Zhou et al. (2022), Raichoor et al. (2020), and Yèche et al. (2020).

However, this paper refers extensively to the earlier papers (Yèche et al. 2020; Chaussidon et al. 2021) that reported the method to select the quasars in DESI and the methodology to model and correct the variations in the target densities. We also refer the reader to Dey et al. (2019) for a detailed description of photometric imaging from the DESI Legacy Imaging Surveys used in this work, and to Alexander et al. (2022) for a presentation of the QSO control sample obtained after visual inspection.

The outline of this paper is as follows. Section 2 presents the photometric data, both in optical and infrared bands, used to select the quasar targets. The QSO target selection of the main survey is detailed in Section 3. We describe in Section 4 the photometric properties of the main selection, i.e., the variations in the target densities as a function of parameters characterizing the photometric catalogs. In Section 5, we present all the extensions of the main selection or the alternative methods of quasar selection tested during the first phase of SV. Section 6 shows how we derived the optimal selection from the results of the SV. Finally, Section 7 presents the results obtained with the main selection over the 1% survey and the first 2 months of the main survey. We conclude in Section 8.

2. Imaging for DESI

To select targets for the DESI spectroscopic survey, the Legacy Imaging Surveys DR9[42] program was conducted over more than 19,700 deg^2 of extragalactic sky visible from the Northern hemisphere, in three optical bands g (470 nm), r (623 nm), and z (913 nm). A large fraction of this area (14,750 deg^2) was observed with at least three passes. The size of the final DESI footprint will be around 14,000 deg^2 and it will be chosen in this region. A full description of the Legacy Imaging Surveys is available in Dey et al. (2019). The optical bands were collected via three independent programs:

1. The Beijing–Arizona Sky Survey (BASS) observed ∼5100 deg^2 of the north Galactic cap (NGC) in g and r using the 2.3 m Bok telescope (Zou et al. 2017). The area surveyed corresponded to approximately decl. > 32.375 deg.
2. The Mayall z-band Legacy Survey (MzLS) provided z-band observations over the same footprint as BASS using the 4 m Mayall telescope. Because the median value of the point-spread function (PSF) size is significantly better than in the BASS data, the MzLS data are critical for deblending sources and deriving source morphology.
3. The Dark Energy Camera Legacy Survey (DECaLS) was performed with DECam (the Dark Energy Camera) on the 4 m Blanco telescope. DECaLS observed the bulk of the Legacy Imaging Surveys footprint in g, r, and z. DECam was initially built to conduct the Dark Energy Survey (DES) and DECaLS expanded the DES area using publicly available DECam time. DECaLS incorporates imaging in the DES footprint, but the DES imaging is significantly deeper as it is covered by more exposures (more than four in each band) than standard DECaLS observations.

[42] https://www.legacysurvey.org/dr9/

Table 1
Median Values of the PSF Depth and Size for the Three Imaging Surveys That Together Constitute the DR9 Legacy Imaging Surveys

	PSF Depth (mag)			PSF Size (arcsec)		
	g	r	z	g	r	z
DECaLS (non-DES)	24.7	24.2	23.3	1.51	1.38	1.31
DES	25.2	25.0	23.8	1.42	1.24	1.14
BASS	24.2	23.7		1.89	1.67	…
MzLS	…		23.3	…	…	1.24

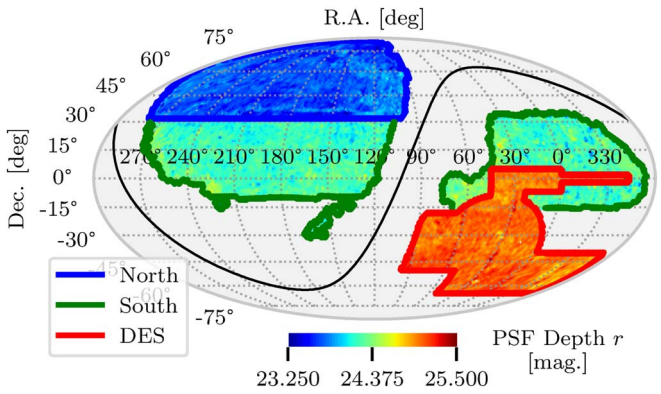

Figure 1. Distribution of the PSF depth r in the DR9 Legacy Imaging surveys footprint. The r band is used to define the magnitude limit for DESI QSO target selection. The solid black line shows the Galactic plane. Three different imaging footprints are highlighted. The blue region represents the combination of BASS and MzLS (designated as the North region in this paper). The red region represents the DES part of DECaLS. The green region, which excludes the red and blue regions, represents the non-DES part of DECaLS. The union of the red and green regions is referred to as the South region in this paper.

The Legacy Imaging Surveys include an overlap region in the NGC for decl. ∼ 32°, which allows us to compare the north imaging (BASS+MzLS) and the south imaging (DECaLS) and to study the target selection performances for the different surveys. The median values of the PSF depth and size that quantify the quality of the photometry are given in Table 1 for each program. Figure 1 shows the PSF depth r in the Legacy Imaging Surveys and highlights three distinct regions:

1. In blue, the combination of BASS and MzLS covering the northern part of the DESI footprint with decl. > 32°.375, (∼5100 deg^2), (designated as North hereafter).

2. In red, the DES part of DECaLS covering ∼4600 deg^2 (designated as South DES hereafter).
3. In green, the non-DES part of DECaLS covering ∼9900 deg^2 (designated as South non-DES hereafter).

The optical survey was complemented by two infrared bands from the all-sky data of the WISE satellite (Wright et al. 2010), namely, W1 (3.4 μm) and W2 (4.6 μm). By using Tractor (Lang et al. 2016) and by matching WISE to deep optical imaging, one can partially deblend the images of confused WISE sources and significantly improve the signal-to-noise ratio of the WISE photometry and color measurements. Our unWISE coadds (Meisner et al. 2017) preserve the native WISE resolution and typically incorporate ∼4 × more input frames than those of the AllWISE Atlas stacks (Cutri et al. 2021).

DECaLS also include W1 and W2 forced photometry light curves corresponding to all optically detected sources. These light curves are measured from time-resolved coadds similar to those described in Meisner et al. (2017). Such light curves provide information on the variability of all optically detected sources, which were tested for use as part of the DESI quasar selection during SV (see Section 5). In DR9, the Legacy Surveys W1 and W2 light curves typically have 15 coadded epochs per band, spanning a ∼10 yr time baseline.

3. Quasar Target Selection

In this section, we describe the target selection used in the 1% survey and the main survey. This selection corresponds to bit 2 (QSO) of the maskbits SV3_DESI_TARGET and DESI_TARGET described in Myers et al. (2022).

3.1. Overview of the Sample

The DESI survey uses QSOs as point tracers of the matter clustering mostly at redshifts lower than 2.1, in addition to using QSOs at higher redshift as backlights for clustering in the Lyα forest. This approach expands the role of QSOs relative to the BOSS project (Ross et al. 2012), which only selected QSOs at $z > 2.15$ for use via the Lyα forest, and enhances their role relative to eBOSS (Myers et al. 2015), where QSOs are used in a similar fashion as in DESI although with lower densities.

In DESI Collaboration et al. (2016a), based on the quasar luminosity function (QLF) of Palanque-Delabrouille et al. (2016), we inferred that a complete QSO sample, brighter than magnitude $r = 22.7$, would contain about 190 QSOs per deg^2 at $z < 2.1$ and about 70 at $z > 2.1$. Assuming a minimum efficiency of about 65%, the goal of DESI was to obtain the redshifts for 120 and 50 QSOs per deg^2 in the redshift ranges $z < 2.1$ and $z > 2.1$, respectively. With the SV during which we were able to test several extensions of our selection, we demonstrated that we can significantly exceed these statistics without significantly inflating our target budget (see Section 6). Therefore, in the main selection presented in this section, we use a magnitude limit of $r = 23.0$ for an average density of ∼310 targets per deg^2.

3.2. Strategy for the Selection

QSOs commonly exhibit hard spectra in the X-ray wavelength regime, bright Lyα emission in the rest-frame UV, and a power-law spectrum behaving as $F_\nu \propto \nu^\alpha$ with $\alpha < 0$ in the mid-infrared bands (Stern et al. 2005; Donley et al. 2012). In the mid-optical colors, QSOs at most redshifts are not easily distinguished from the much more numerous stars. Successful selection of a highly complete and pure QSO sample must make use of either UV or infrared photometry. With the extended (WISE) mission that more than quadrupled the exposure time of the original (WISE) all-sky survey, and in the absence of any "u"-band imaging over the whole DESI footprint, we decided to rely upon optical and infrared photometry for QSO selection.

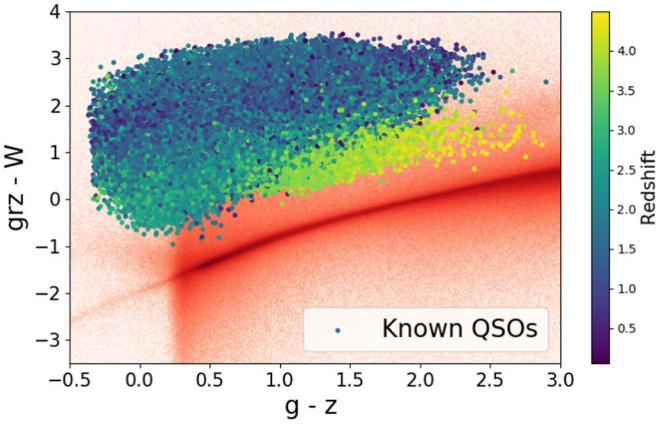

Figure 2. Colors in the optical or near-infrared of objects photometrically classified as stars (red) or spectroscopically classified as QSOs (from blue to yellow dots, depending on their redshift). The color $grz - W$ allows us to reject stars based on the *infrared excess* of QSOs.

Therefore, the DESI QSO target selection is a combination of optical-only and optical+IR colors. In order to illustrate this strategy, we use two colors, $grz - W$ versus $g - z$ where grz is a weighted average of the grz band fluxes with flux(grz) = [flux(g) + 0.8 × flux(r) + 0.5 × flux(z)]/2.3 and W a weighted average of W1 and W2 fluxes with flux(W) = 0.75 × flux(W1) +0.25 × flux(W2). In the Legacy Imaging Surveys (Dey et al. 2019), the conversion from linear fluxes to magnitudes is $m = 22.5–2.5 \log_{10}$(flux). Figure 2 shows the bulk of the QSO targets that are identified in an optical+IR selection where the excess infrared emission from QSOs results in a clear segregation from stars with similar optical fluxes. Stellar spectral energy distribution (SEDs) indeed sample the rapidly declining tail of the blackbody spectrum at those wavelengths, where QSOs have a much flatter SED than stars. This method was previously demonstrated in eBOSS, and Figure 5 of Myers et al. (2015) exhibits the same separation between stars and QSOs thanks to WISE imaging.

3.3. Selection with a Random Forest Algorithm

Neural-network-based algorithms implemented in BOSS (Yeche et al. 2010) were found to increase QSO selection efficiency by ≈20% compared to color cuts. Similarly, to improve the success rate for DESI, we use a machine-learning algorithm based on random forests (RFs).

First, before utilizing the RF, we restrict the selection to objects with stellar morphology ("PSF" in DR9), to avoid an almost 10-fold contamination by galaxies that otherwise enter our selection region, and we impose $16.5 < r_{AB} < 23.0$. In addition, to reject stars, we apply a cut on the (WISE) magnitudes (W1 < 22.3 and W2 < 22.3). This cut is particularly efficient at getting rid of stars in the Sagittarius stream, a region that exhibits an overdensity of QSO targets (see Figure 3 and discussion in Section 4.1). We also require that the targets

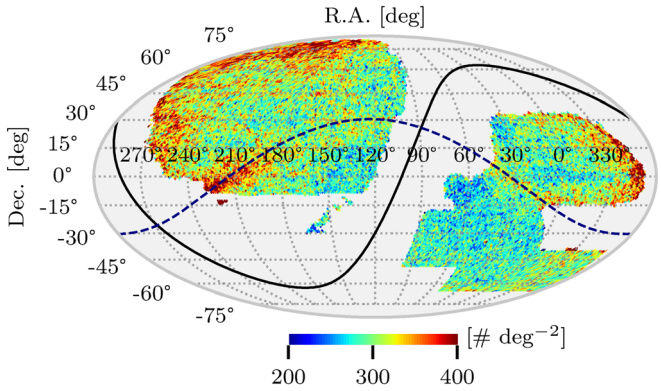

Figure 3. Density map of the DR9 QSO target selection. The solid black and dashed blue lines show respectively the Galactic plane and the plane of the Sgr stream.

are not in the vicinity of bright stars, globular clusters, or large galaxies. Such *masked* sources have `MASKBITS` of 1, 12, or 13 set in Legacy Surveys catalogs.

Then, we train the RF using two samples: one of *QSOs* similar to the objects we want to select and the other of *stars* we want to discriminate against. The QSO sample consists of 332,650 known QSOs in the DESI footprint. The vast majority of those QSOs with $17.5 < r < 23.2$ are selected by their intrinsic time variability in the SDSS Stripe 82 (an equatorial stripe in the south Galactic cap (SGC) defined by SDSS), using the method described in Palanque-Delabrouille et al. (2011) with SDSS light curves. This selection provides a training sample of QSOs that is not biased by information on QSO color, an essential ingredient for the RF training. The *star* sample is obtained by considering 332,650 unresolved sources in Stripe 82 that are not known QSOs and do not exhibit any QSO-like variations in their SDSS light curve. We randomly select the stars from this much larger sample such that the *r*-band number counts of the stars match the QSOs. We train the RF selection with 11 input parameters: the 10 possible colors using the five optical and NIR bands *grzW1W2*, and the *r*-band magnitude. In contrast to the RF method applied during the DESI commissioning (Yèche et al. 2020), the final selection uses a single RF covering the full QSO redshift range, which we retrained with the latest processing of imaging catalogs, DR9.

In order to achieve the required QSO target budget, ∼310 targets per deg^2, and to ensure a uniform target density over the full DESI footprint, we apply slightly different thresholds on the RF probability in the three regions (North, South (DES) and South (non-DES)), see the exact definition in Figure 1). We also vary the RF probability threshold with *r*, following $p_{\rm th}(r) = \alpha - \beta \times \tanh(r - 20.5)$. For the three regions (North, South (DES), and South (non-DES), we choose (α, β) to equal (0.88, 0.04), (0.7, 0.05), and (0.84, 0.04), respectively.

The code for the QSO target selection of both the 1% survey and the main survey is publicly available on GitHub and it is available at 1% QSO selection and main QSO selection.

4. Photometric Properties of the QSO Selection

In this section, we discuss the spatial uniformity of the QSO target density for the main selection described in Section 3. We also present the density fluctuations related to photometric properties such as seeing and depth. The mitigation procedure to remove the systematic effects is described in detail in detail in Chaussidon et al. (2021).

4.1. Quasar Target Density

Figure 3 exhibits several regions with a higher density of QSO targets than average:

1. Overdensity near the Galactic plane: the stellar density is higher near the Galactic plane (black line in Figure 3), which increases the stellar contamination of the QSO targets. The effect is mostly visible in the region bounded by $270° < \mathrm{R.A.} < 330°$ in both the NGC and SGC.
2. Overdensity in the Sgr stream: the stellar population of the Sgr stream, indicated by the dashed blue line in Figure 3, is different from the Galactic stellar population. Most of the stars in the Sgr stream are bluer than Galactic stars and tend to have similar colors to the bulk of the QSO population. We empirically noted that Sgr stream stars are very faint in the two NIR bands, W1 and W2, compared to Galactic plane stars, which justifies our NIR cut ($W1 < 22.3$ and $W2 < 22.3$) in Section 3. This overdensity is mainly visible in the NGC but it can also be observed in the SGC at $0° < \mathrm{R.A.} < 30°$.
3. Overdensity in the North: the QSO target density increases with decl. This overdensity could be due to the poorer PSF depth in the *z* band in this region. This is likely caused by imaging depth decreasing at higher decl. due to increasing airmass, which was not fully compensated for by additional exposure time in the MzLS observing strategy. Since the *z* band plays a crucial role in the QSO selection, the discriminating power between stars and QSO targets is reduced at higher decl.

The DES footprint, which benefits from a 1 mag deeper photometry in all optical bands is, as expected, the least contaminated region.

4.2. Systematics

4.2.1. Observational Parameters Governing the QSO Target Density

All the important observational parameters governing the QSO target density are described in Chaussidon et al. (2021). We give a brief summary of these parameters below:

1. Stellar density [deg^{-2}]: Density of point sources from Gaia DR2 (Gaia Collaboration et al. 2018) in the magnitude range $12 < \texttt{PHOT\_G\_MEAN\_MAG} < 17$.
2. $E(B - V)$ [mag]: Galactic extinction from Schlegel et al. (1998) as modified by Schlafly & Finkbeiner (2011).
3. Sgr stream [arbitrary unit]: Stellar density in the Sgr stream derived from Antoja et al. (2020). This number is defined as the ratio of the number of stars in the pixel over the mean number of stars per pixel.
4. PSF depth [1/nanomaggies^2] in *r*, *g*, *z*, W1, W2: the 5σ point-source magnitude depth.
5. PSF size [arcsec] in *r*, *g*, *z*: seeings, inverse noise-weighted average of the FWHM of the PSF.

4.2.2. Systematic Effects

Figure 4 shows the relative QSO target density as a function of each observational parameter, allowing us to identify the main sources of systematic effects in the QSO target selection. We observe very different behaviors in the three regions.

In the South (DES) region, because of the deeper photometry in optical bands, all the fluctuations of the relative density are at

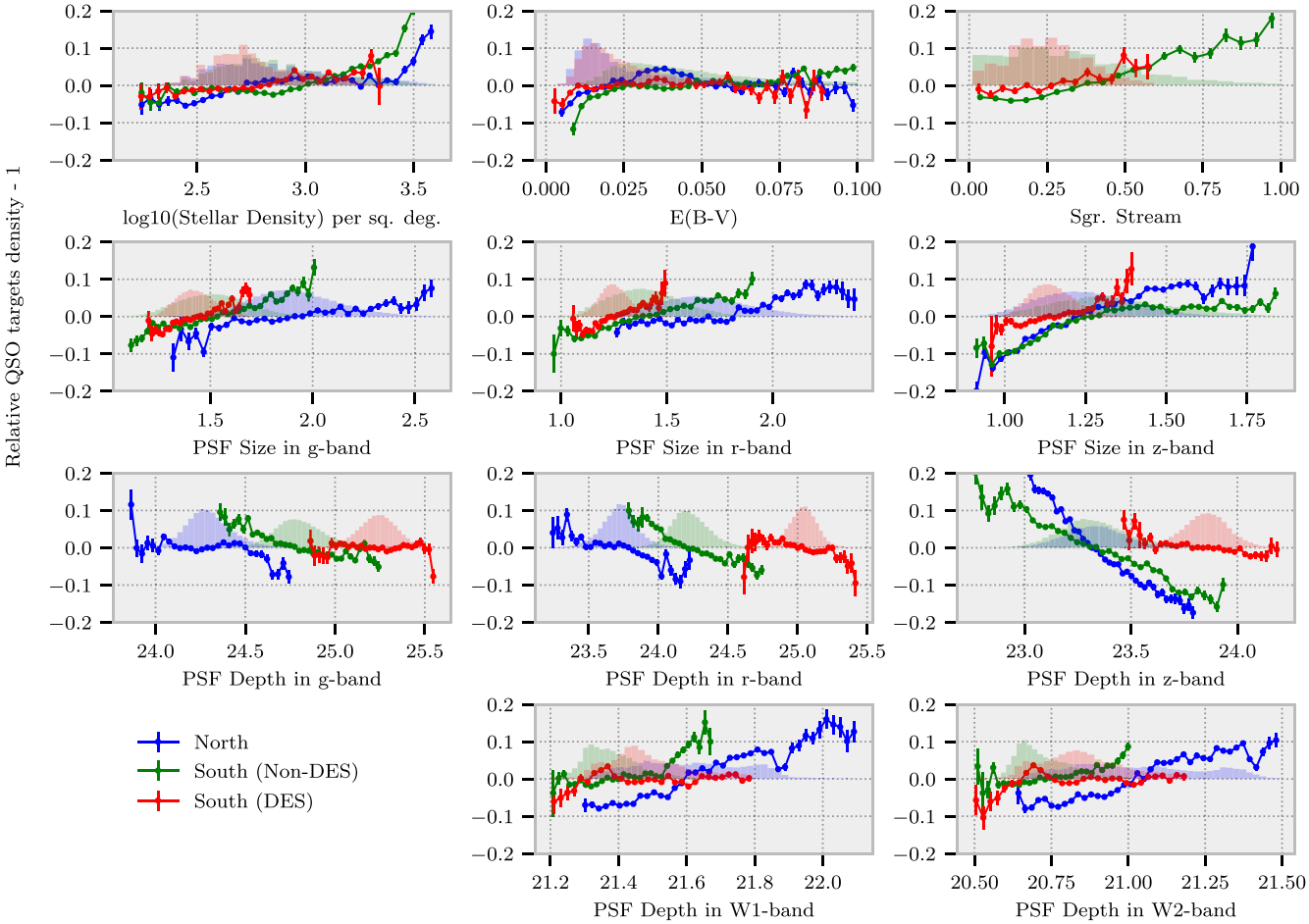

Figure 4. Relative QSO target density in the North, South (non-DES), and South (DES) regions as a function of each observational parameter (see Section 4.2.1 for the definition of the parameters). The relative QSO target density is a mean value after rejecting outliers. The histograms represent the distributions of each observational parameter in the three regions. The color code is blue, green, and red, respectively, for the North, South (non-DES), and South (DES) regions.

the order of only a few percent, typically, one order of magnitude below the level of fluctuations in the other two regions (North and South (non-DES)).

In the North region, the morphology is driven by the z band since the MzLS telescope is the one with the best seeing. In addition, the segregation between stars and QSOs is based on the comparison of the optical z band with the two NIR (W1, W2) bands. Therefore, we observe a strong dependence of the QSO density on the z-band seeing as well as on the z, W1, and W2 depths.

In the South (non-DES), we observe the same trends except that the QSO density is less sensitive to the z-band seeing because the morphology is determined from an almost balanced combination of the three optical bands. Finally, the W1 and W2 imaging is shallower in the South region compared to the North one because WISE produced many more images around the North Ecliptic Pole located in the North region. However, the behavior is essentially the same: the blue and green curves (see Figure 4) are just shifted by $\sim$0.5 mag.

5. Extended Selection of QSO Targets During SV

The goals of the first SV phase were to optimize the selection algorithms, estimate the redshift distributions, and evaluate the projected cosmological constraints. In this section, we describe the extensions of the main selection and the alternative QSO selection methods that we tested during SV.

In practice, as explained in Section 5.1, we varied the definition of the stellar morphology and the magnitude limit. We released the cuts on the RF probability and on the definition of the color boxes. The goal was to select fainter QSOs or those with higher redshift missed by the main selection. In parallel, we tested new algorithms using, for instance, the intrinsic variability of the QSOs. All these variations of selections are grouped into five classes, which are described in Section 5.2.

5.1. Alternative Selections

5.1.1. Source Morphology for the Quasar Selection

The first SV study was related to the definition of stellar morphology ("PSF" in DR9). Figure 5 shows the potential gain that we expect using point-like sources in the COSMOS/HST (Hubble Space Telescope) region. For instance, we can extend the definition of "PSF" sources to also include objects photometrically classified as *extended* but having a small relative χ^2 difference between PSF and extended morphological models ($\Delta(\chi^2)/\chi^2 < 0.015$). Using the DR9 Legacy Surveys Imaging catalogs, the relative χ^2 is defined as (`dchisq[''REX'']-dchisq[''PSF'']`)/`dchisq[''PSF'']`.

In Section 6, we will discuss the impact of these extensions and the optimization performed to achieve the final main selection discussed in Section 3. For instance, in this specific case, we will study the redshift distribution of the QSOs

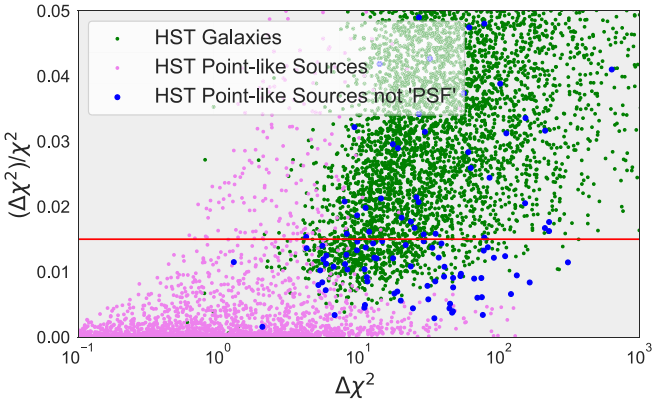

Figure 5. Relative χ^2 difference between extended and "PSF" models as a function of the χ^2 difference, for COSMOS/HST objects. The violet dots correspond to objects confirmed as point-like sources in HST imaging. The green dots correspond to objects identified as extended galaxies in the HST imaging. The blue dots are HST point-like sources that are classified as extended objects in the DECaLS DR9 photometric catalogs.

recovered with the looser morphology restriction. It will allow us to assess the trade-off between a higher QSO completeness and an increase in the quasar target budget.

5.1.2. Extension of the Color Selections

In parallel, we investigated two approaches for the QSO selection, one based on color cuts and the other on a machine-learning algorithm. At the time of the SV, both methods had reached a high level of maturity, and one of the SV goals was to select between the two approaches (Yèche et al. 2020). In addition to the pure performance in terms of the number of true quasars selected per square degree for a given target budget, the relative sensitivity to systematic effects also has to be assessed. Finally, if the sample of spectroscopically confirmed quasars selected by one of the two approaches is included in the sample selected by the other approach, we will retain the selection yielding the largest set of validated quasars.

The QSO luminosity function indicates that the size of the QSO samples at both $z < 2.1$ and $z > 2.1$ can be increased by extending the magnitude limit above $r = 22.7$. The benefits are particularly apparent for the higher redshift Lyα forest QSOs. Therefore, we relaxed the magnitude limit to $r = 23.2$ for the extended SV RF selection, as shown by the distribution of r-band magnitude in the "Ext. Random Forest Selection" in Figure 6. We also developed an additional selection for Lyα forest QSOs as faint as $22.7 < r < 23.5$ (see the distribution of r-band magnitudes of the "High-z and Faint Selection" in Figure 6). In addition, a goal of SV was to determine how efficiently we can identify and classify high-redshift quasars with these extended selections for the nominal effective exposure time, $T_{\rm eff} \sim 1000$ s (see definition in E. F. Schlafly et al. 2022 in preparation).

5.1.3. Selection of High-z QSOs

QSOs at $z > 5$ provide direct probes of the evolution of the intergalactic medium and supermassive black holes at early cosmic times. Current high-redshift QSO surveys either mainly focus on the bright end or are limited to a small deep field. We conducted a selection for $z \gtrsim 5$ faint QSOs using photometry from DECaLS grz and unWISE W1, W2. The selection method is based on the color selections that have been used in previous

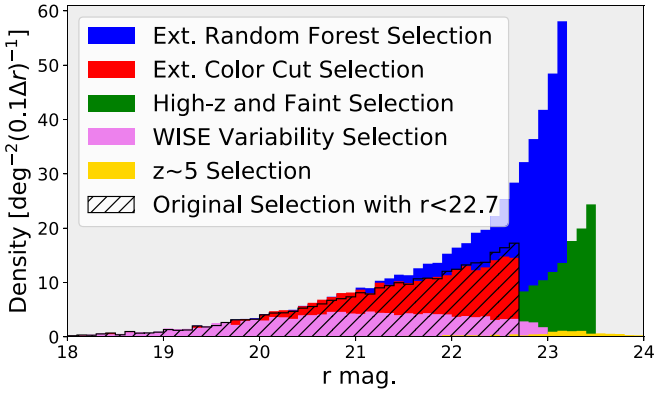

Figure 6. Target densities as a function of the r magnitude for the five classes of extended SV selections and the original selection with $r < 22.7$. All the selections are based on DECaLS DR9 imaging catalogs.

successful $z \sim 5$–6 QSO surveys (Wang et al. 2016; Yang et al. 2017). The main techniques are g-band/r-band dropout and the $r - z/z - W1$ color–color diagram. The unWISE W1 − W2 color is used to further reject M dwarfs. We have a survey depth of z-band magnitude 21.4. We divide the selection into two sets based on two redshift ranges, $z_{\rm red} \geqslant 4.8$ and $4.3 < z_{\rm red} < 4.8$, and apply different color cuts according to QSO color-$z_{\rm red}$ tracks in $r - z/z - W1$ and W1 − W2 color space.

5.1.4. WISE Variability Selection

Finally, in Palanque-Delabrouille et al. (2011), it was demonstrated that the SDSS light curves on the stripe 82 provide a very efficient method to select the QSOs by their intrinsic variability. The DR9 (WISE) catalog offers, for each object, light curves with 15 epochs over a time period of about 10 yr in the W1 and W2 bands. We adapted the method developed in Palanque-Delabrouille et al. (2011) to the (WISE) light curves. We selected objects with "PSF" morphology and $18.0 < r < 23.0$, passing a low RF probability cut, $p > 0.1$, and exhibiting a high variability in their light curves. This variability technique is a robust, efficient, and well-understood method, less sensitive to the spatial nonuniformity of the optical imaging. The goal was to study whether such a method can select quasars not already spotted by the usual methods based on optical and NIR colors.

5.2. Definition of the QSO Target Maskbits and Links to the Public Code

We defined five classes of quasar selection for SV, grouping the extensions described above. Each selection can be identified by a combination of bits of SV1_DESI_TARGET defined in Myers et al. (2022). The code for the QSO target selection of SV is public on GitHub and a link to the code is provided for each class.

1. Extended color cut selection, `QSO_COLOR_4PASS` or `QSO_COLOR_8PASS` (∼300 deg^{-2}): Compared to the color cut selection of Yèche et al. (2020), we relaxed all the definitions of the color boundaries; loosened the veto on the color box defined for stars, and applied a looser selection when requiring point-source morphology. Link to the code.

2. Extended random forest selection, QSO_RF_4PASS or QSO_RF_8PASS (∼570 deg^{-2}): Compared to the RF selection of Yèche et al. (2020), the r-band magnitude limit is extended to $r = 23.2$, the RF probability is reduced, and a looser selection is applied to require point-source objects. Link to the code.
3. High-z and faint QSO selection, QSO_HZ_F (∼115 deg^{-2}): The selection is extended to fainter objects $22.7 < r < 23.5$. We have also applied a looser cut on the RF probability than for the nominal selection but with an additional color cut to enhance the fraction of high-z QSOs. Link to the code.
4. $\mathbf{z \sim 5}$ QSO selection, QSO_Z5 (∼20 deg^{-2}): We use g-band and r-band dropout techniques to select very high-z QSO candidates ($4.5 < z_{\rm red} < 5.5$). Link to the code.
5. WISE variability selection, WISE_VAR_QSO in secondary targets SV1_SCND_TARGET (∼140 deg^{-2}): We use the intrinsic variability of the QSOs, based on the WISE light curves spanning over 10 yr.

The r-band magnitude distribution for each class is shown in Figure 6. Many objects are common to the different classes and the total density is not the simple sum of all the individual densities. Finally, the overall density is of the order of 700 targets per deg^2, to be compared to 260 targets per deg^2 for the original selection.

6. Optimization of Quasar Selection with SV

In this section, we describe our process to build a catalog of QSOs using the DESI spectroscopic information for each of the QSO targets we observed. We validate the catalog with a control sample of QSOs obtained after visual inspection of the spectra (Alexander et al. 2022). We then use this catalog to optimize the QSO selection (definition of point sources, magnitude limits, etc.) and we test the impact of the alternative selections (color cut selection, (WISE) variability, etc.) proposed in Section 5. For each alternative selection, we present its results and we estimate the potential gain in terms of QSO density by reference to the total target budget. Finally, we explain our choice of QSO selection for DESI, which is described in Section 3.

6.1. Data Set and Visually Inspected Control Sample

The first phase of SV was used to optimize the QSO target selection. In this section, we study 45 fields observed during this phase. They contain a mix of luminous red galaxies, emission line galaxy targets, and quasar targets (see Table 2). Among them, 42 fields have a total effective exposure time of $T_{\rm eff} \sim 4000$ s and three fields correspond to ultra-deep observations ($T_{\rm eff} = 7200$, 10,820, 8200 s) (see a few examples of spectra in Figure 7).

The latter observations have been visually inspected and those three fields provide a pure sample of QSOs that we use as a control sample when building the QSO catalog (see Section 6.2). The breakdown of the visual inspection results is summarized in Table 3. As the main purpose of SV selection was to collect all the possible QSOs, the selection was extremely loose and we cannot draw any conclusion about the contaminants.

By contrast, the second row of Table 3 gives us a description of the contaminant of the QSO main selection. Roughly, one-quarter of the contaminants are stars and the other three-quarters are galaxies. The fraction of contaminant increases for fainter targets, especially for galaxies as illustrated in Figure 8. Comparison of Figures 2 and 9 shows that the location in the color–color space, of the two contaminants, stars and galaxies, are in the middle of the QSO color space, demonstrating the difficulties in improving the QSO selection.

Table 2
Description of the Three Data Sets (First SV Phase, 1% Survey, Main Survey) Used in This Paper for QSO Analysis

	Number of Fields	Effective Area (deg^2)	Number of Good Spectra	Number of QSOs
First SV phase	45	90.5	78,182	26,094
1% survey	79	159.6	53,307	33,813
Main survey	305	1290.9	432,383	264,753

Note. For the 1% survey, we only study the fields with an effective area greater than 0.4 deg^2.

6.2. Quasar Catalog

The process to produce the QSO catalog is illustrated by the flowchart in Figure 10. The method is based on three algorithms: the DESI pipeline classifier Redrock (RR), a broad Mg II line finder (Mg II), and a machine-learning-based classifier QuasarNET (QN).

The RR algorithm (S. J. Bailey et al. 2022 in preparation) is a template-fitting classifier. It uses a set of templates for each class (star, galaxy, or QSO) constructed from spectra observed in SDSS. After PCA decomposition, these templates provide a linear basis. Linear combinations of the basis components are fitted to each spectrum for each redshift within a suitable range. From these fits, a best class and a best redshift are determined, corresponding to the template class-redshift combination that resulted in the lowest $\Delta\chi^2$. Therefore, as an output, RR provides both the class of the object (star, galaxy, or QSO) and its best-fit redshift.

The Mg II algorithm identifies spectra with a Mg II broad line. It is an afterburner, run after RR and using RR outputs as inputs. The goal is to change the initial classification of the object from Galaxy to QSO if the spectrum exhibits a Mg II broad line. The method consists in fitting a Gaussian in a 250 Å window centered at the position of Mg II line given by RR. We consider the Mg II line as a broad line if the improvement of χ^2 is better than 16, the width of the Gaussian greater than 10 Å, and the significance of the amplitude of the Gaussian greater than 3. The algorithm possibly changes the source classification but never modifies the redshift given by RR.

The QN algorithm (Busca & Balland 2018; Farr et al. 2020) is a deep convolutional neural network (CNN) classifier, taking a smoothed spectrum as an input before carrying out four layers of convolutions. The output from these convolutions is then passed to a fifth, fully connected layer, before feeding into a number of *line finder* units. Each of these units consists of a fully connected layer, trained to identify a particular emission line. In our case, we use the following six lines: Lyα, C IV, C II, Mg II, Hα, and Hβ, and an object is classified as a QSO if at least one of the six confidence probabilities is greater than 0.5.

Our strategy to build the final QSO catalog was established thanks to a control sample of QSOs obtained by visual inspection of their DESI spectra (Alexander et al. 2022). This

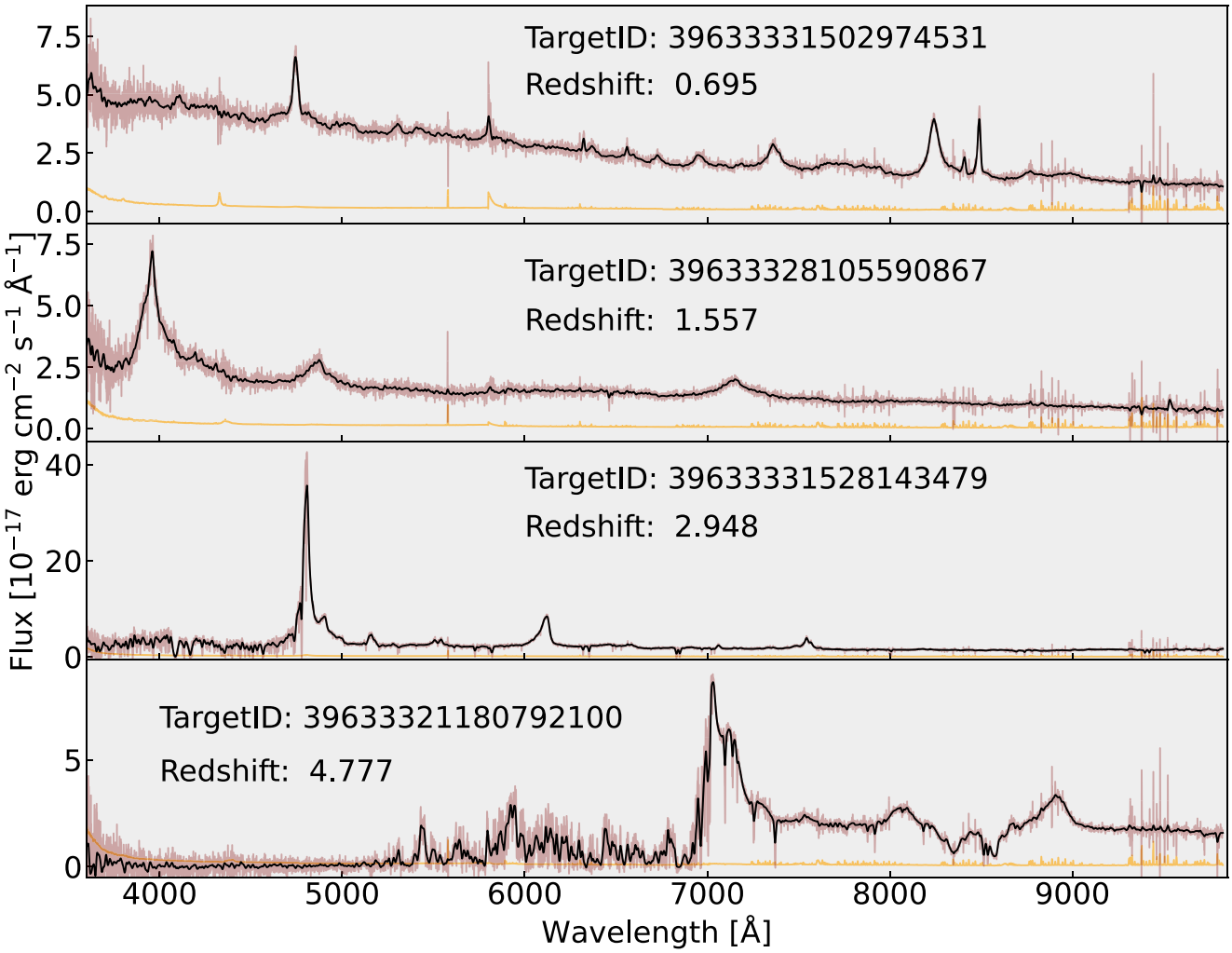

Figure 7. Four spectra of the ultra-deep field used for visual inspection. The field is centered at R. A. = 106.°740 and decl. = 56.°100. The effective exposure time is $T_{\rm eff}$ = 10,820 s. The spectra cover the range of redshifts observed in DESI. The redshifts are 0.695, 1.557, 2.948, and 4.777. The last spectrum is a very rare case of a target selected by both the RF and the high-z selections. The maroon curves represent the DESI spectra. The black curves are obtained after smoothing the spectra with a Gaussian filter. The orange curves represent the noise spectrum.

Table 3
Fractions of the Spectrum Types for the Three Ultra-deep Fields That Were Visually Inspected

	Fraction of QSOs	Fraction of Stars	Fraction of Galaxies	Fraction of Inconclusive
SV sel.	33.5%	11.9%	39.8%	14.8%
Main sel.	71.0%	6.3%	16.1%	6.7%

Note. Spectra that are of insufficient quality to assign a type are labeled "inconclusive." The first and second rows are, respectively, for the SV and main selections.

truth sample contains ∼1330 QSOs passing the selection summarized in Section 5, see the results in Table 3.

In order to monitor the quality of our catalog, we define two quantities, the efficiency and the purity. Those two parameters are performance metrics similar to parameters used in classification problems (Powers 2011), respectively, the recall and the precision. We define the efficiency, ε, as the fraction of the QSOs of the control sample that is selected in the catalog and the purity, p, as the fraction of the catalog objects confirmed as QSOs. Numerically, the ε and p are defined as

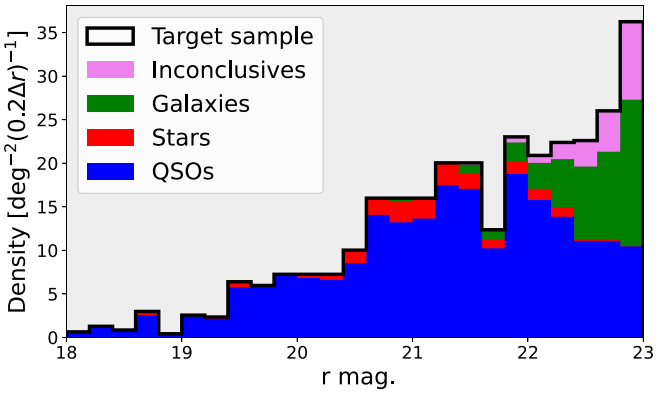

Figure 8. Composition of the main selection.

$\varepsilon = N_c^{\rm QSO}/N_{\rm cs}^{\rm QSO}$ and $p = N_c^{\rm QSO}/N_c$, where $N_c^{\rm QSO}$, $N_{cs}^{\rm QSO}$, and N_c are, respectively, the number of QSOs in the catalog, the number of QSOs in the control sample, and the number of objects in the catalog.

Figure 11 shows the performance achieved when the RR, Mg II, and QN algorithms are successively applied. From Figure 11, we learn that by using the QSO class from RR alone,

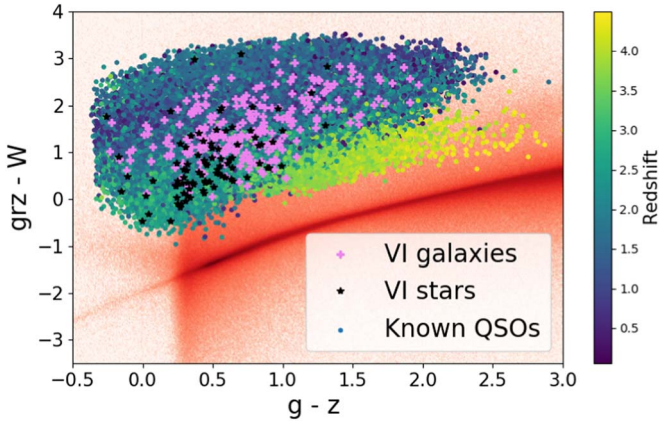

Figure 9. Colors in the optical or NIR of objects photometrically classified as stars (red) or spectroscopically classified as QSOs (from blue to yellow dots, depending on their redshift). The black stars and the violet crosses correspond, respectively, to star and galaxy contaminants.

we obtain a catalog with a very high purity and an efficiency of the order of 80%. Adding the QSOs identified by Mg II algorithm, low-z QSOs are recovered. Finally, the QN algorithm allows us to recover faint QSOs missed by the RR or Mg II algorithms. For the main selection described in Section 3, the total efficiency and purity are respectively $99.2\% \pm 0.3\%$ and $98.3\% \pm 0.4\%$. These results reflect the performance of the QSO catalog that will be used in the DESI science analyses and not the composition of the parent QSO target sample described in Table 3 and in Figure 8.

For the contaminants of the catalog, we have limited statistics, only 17 spectra. Therefore, it is difficult to draw definitive conclusions. Of the 17 spectra, none corresponds to that of a star and eight spectra do not have sufficient quality to assign a type. Of the nine galaxy spectra, all the spectra but one have the correct redshift in the QSO catalog. These objects correspond to a transition phase during which the quasar is formed. Considering those galaxies with a good redshift as good tracers of the matter, the purity increases to $99.1\% \pm 0.3\%$.

To summarize the flowchart in Figure 10, we first classify the object as QSO if it is classified as QSO by RR. We check if the redshift is confirmed by QN, otherwise, we refit the redshift with RR using a top hat prior of ± 0.05 around the redshift given by QN. Then, if the RR classification is GALAXY and the Mg II classification is QSO, we classify the object as QSO and keep the redshift given by RR. Finally, if the object is classified as QSO by QN but neither by RR nor Mg II, we classify it as QSO in the QSO catalog but we refit the redshift with RR using a ± 0.05 top hat prior around the redshift given by QN. In this way, all the redshifts are obtained by a single algorithm, RR, providing a consistent measurement of the redshift.

In summary, we validated the automated QSO catalog with visually inspected objects. We achieve both excellent purity and excellent efficiency. In the rest of this paper, the QSO catalog is therefore built according to the strategy described above. The numbers of QSOs for all the data sets are given in Table 2.

6.3. Source Morphology for the Quasar Selection

The distribution of $\Delta(\chi^2)/\chi^2$ for point-source objects in COSMOS/HST is illustrated in Figure 5. It indicates that we can potentially improve the QSO selection by accepting objects with $\Delta(\chi^2)/\chi^2 < 0.015$. By relaxing the stellar morphology definition in such a way, the target density of the main selection (310 targets per deg^2) is increased by 70 targets per deg^2.

During SV, this option was tested. Figure 12 shows the fraction of additional QSOs selected when relaxing the morphological criterion as a function of the redshift and the r magnitude. The improvement is mainly visible for faint QSOs with $z < 1$, which do not contribute to neither QSO clustering nor Lyα forest studies. In addition, they only add 14 QSOs per deg^2 to a total of 200 QSOs per deg^2 for the main selection.

In conclusion, because the relaxed morphological selection only increases the number of QSOs at low redshifts and because the cost in terms of target budget is significant (+20%), we do not retain this extended definition of stellar morphology and we use the "PSF" morphology definition of DR9 catalogs to select point-like sources.

6.4. Results for the Alternative Selections

The SV phase also allowed us to study several alternative selections described in Section 5. Figure 13 summarizes all the results and compares these alternative methods to the main selection based on an RF approach (see Section 3).

For a fixed target density, ~310 targets per deg^2, the RF selection (main selection) retains 15% more QSOs than the color cut selection on average over all redshifts, and 21% more for the Lyα forest QSOs. Taking the union of the RF and the color cut selections would increase the target budget by 20%. In addition, only 3% of the QSOs selected by the color cut method do not pass the RF selection, and the first row of Figure 13 shows that they mostly have a low redshift. As the vast majority of the QSOs with $z > 1.0$ selected by the color cut method are included in the RF sample, we do not use the color cut selection.

A selection based on the detection of the QSO intrinsic variability with the WISE light curves represents a very interesting alternative because it shows a better spatial uniformity. However, the conclusions are similar to those of the color cut selection. The union with the main selection would increase the target budget by 15% with a QSO gain of 3%, mainly at low redshift (see the second row of Figure 13). Therefore, this selection was not retained.

We have also extended the RF selection to very faint objects $22.7 < r < 23.5$ with an additional color allowing us to select high-z quasars. This selection was extremely expensive in terms of target budgets (+30% for $r > 23.0$) and the gain in terms of QSOs was extremely small, as we can see in the third row of Figure 13, especially for $r > 23.0$. In the main selection, we extended the magnitude limit cut from the original $r = 22.7$ upper bound to $r = 23.0$. In contrast, it was not worth selecting targets above $r = 23.0$.

Finally, this $z \gtrsim 5$ QSO selection has identified ~60 QSOs at $3.9 \leqslant z \leqslant 5.7$ during SV observations. Since at $z \sim 5$ the Lyα emission line is in the i band, color selection that does not include i-band photometry will help construct a sample without dependence on Lyα line luminosity. This selection does identify weak-line and strong broad-absorption-line QSOs missed by the previous $z \sim 5$ selection based on $r - i/i - z$ colors (McGreer et al. 2013; Wang et al. 2016). However, this selection has a high contamination rate due to the lack of i-band data. The success rate is about 2%–3% and most of the contaminants are M dwarfs. About half of the $z \sim 3.9$–5 QSOs

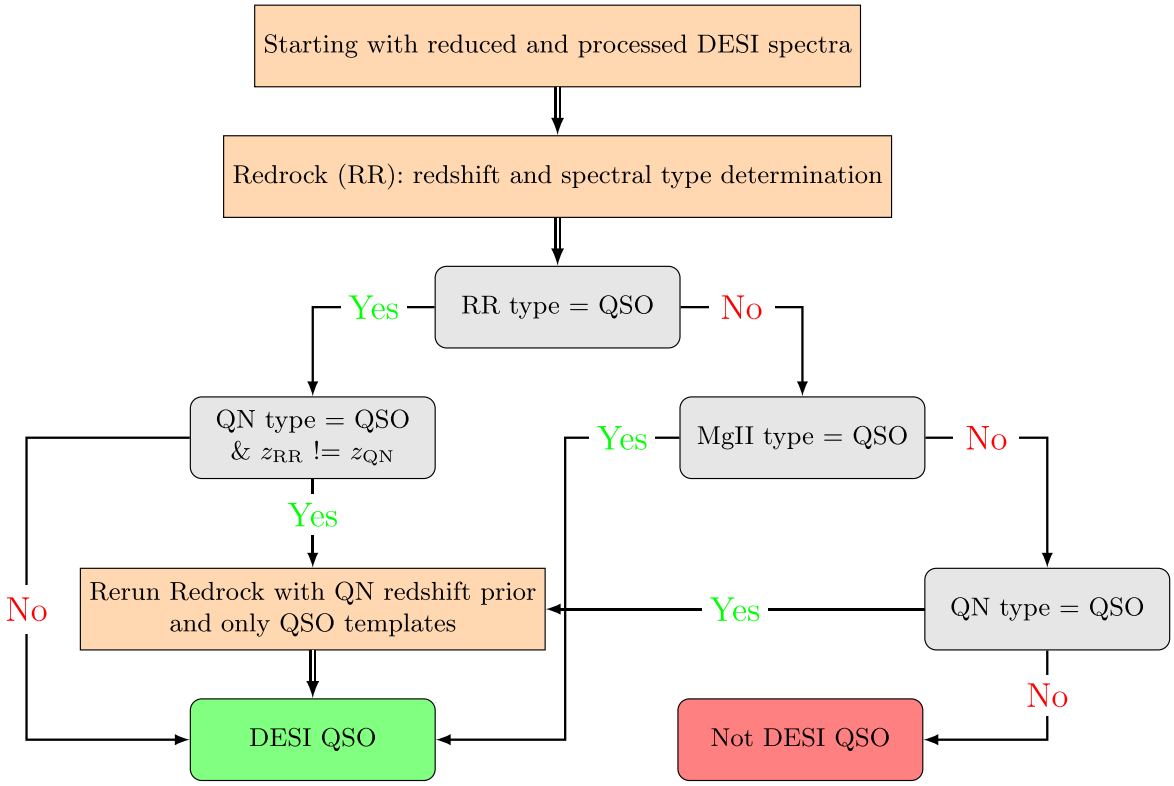

Figure 10. Flowchart to produce the quasar catalog.

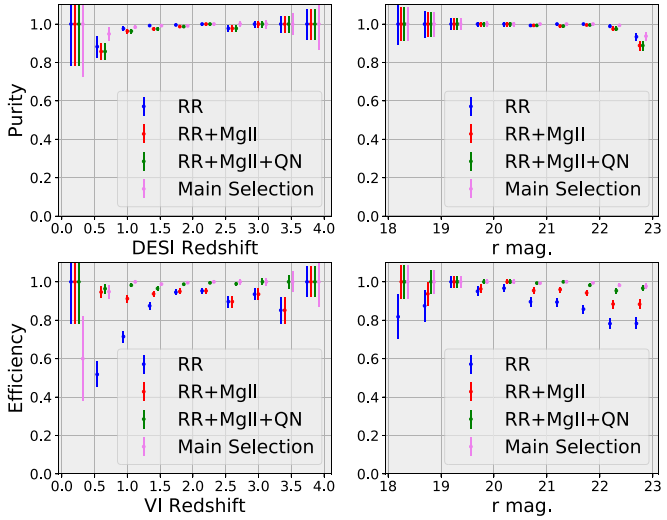

Figure 11. Efficiency and purity as a function of redshift and r magnitude, using the visual inspection catalog as a control sample. The efficiency is the fraction of the control sample that is selected in the catalog. The purity is the fraction of the catalog objects that are confirmed QSOs. Starting with QSO targets selected as described in Section 5, the three algorithms, RR, Mg II, and QN, are successively applied. The violet curve corresponds to the main selection described in Section 3 using the three algorithms (RR+Mg II+QN).

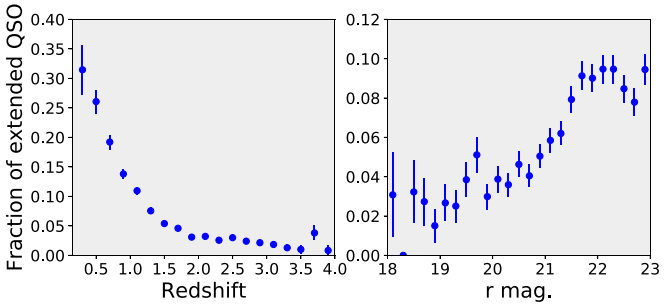

Figure 12. Fraction of additional QSOs selected by relaxing the morphological criterion as a function of the redshift and the r magnitude.

can also be selected by the QSO RF selection. Therefore, this selection is not retained. An updated selection adding i-band photometry from Pan-STARR1 (Chambers et al. 2016) has been developed as a secondary program in the 1% and year 1 main surveys, focusing on QSOs in a higher redshift range, $z \sim 5$–6.5.

In conclusion, all these studies validate the decisions made for the main selection described in Section 3: we select $16.5 < r < 23.0$ objects with a stellar morphology ("PSF" in DR9) and with an RF probability greater than the probability threshold, $p_{\rm th}(r)$. To ensure uniformity of the target density over the whole footprint, $p_{\rm th}(r)$ is optimized independently in each of the three imaging regions.

7. Validation of the Main Quasar Selection in DESI

In this section, we study the performance of the main selection that was deployed both for the 1% and the main surveys. The resulting catalog of QSOs is obtained with the approach presented in Section 6.2.

7.1. Methodology

The instrumental conditions varied a lot during both the SV and the beginning of the main survey. For instance, at the beginning of SV, the fiber reach was limited because of technical developments on the positioners of the focal plane. As a result, only a small fraction of the QSO targets could be observed. This limitation was gradually removed, making data

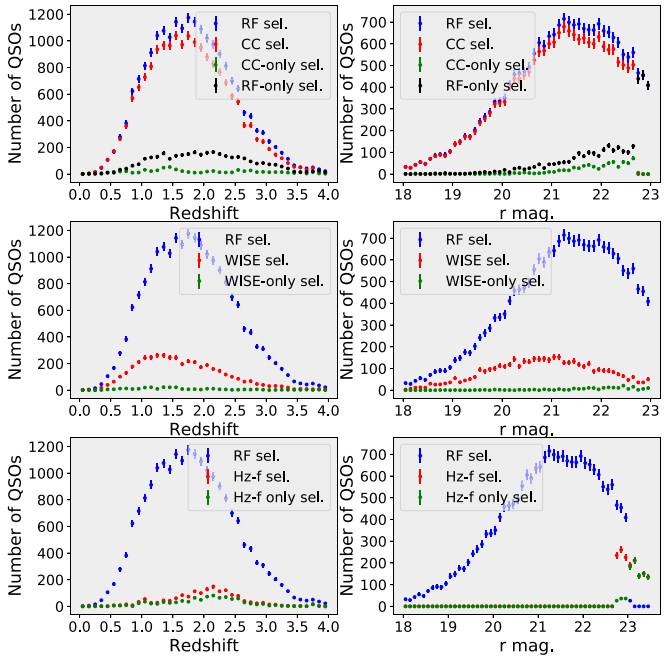

Figure 13. Study of alternative selections. Number of QSOs as a function of the redshift and the r magnitude. Each row of two plots tests successively a color cut selection (CC), a selection based on variability detected in WISE light curves (WISE) and a high-z faint quasar selection (Hz-f).

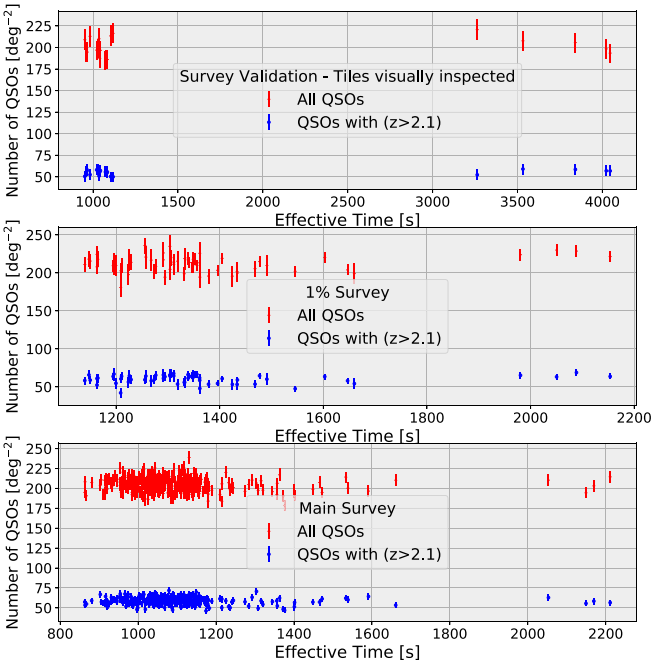

Figure 14. Number of quasars per square degree as a function of the effective time for SV1 (∼1000 or ∼4000 s), the 1% survey, and the main survey. Each point corresponds to a tile.

analysis and the comparison between fields more complex. Similarly, some observations were performed with a subset of only 10 of the spectrographs. To account for the large variability of the instrumental conditions during observations, we use the number of quasars per square degree obtained for each field.

First, for a given field (tile), we compute the effective surface defined as the ratio of the number of QSO targets with a spectrum over the number of QSO targets in the field, multiplied by the surface of the focal plane (8.2 deg^2). Note that the numerator does not include targets that are not assigned to a fiber or for spectra that do not pass the spectroscopic quality flag `COADD_FIBERSTATUS`. The effective surface varies from 1.6 deg^2 for the first tiles of SV, to 4.6 deg^2 for the tiles of the main survey. For the 1% and main surveys, the total effective surfaces are 160 and 1290 deg^2, respectively (see Table 2).

We then divide the number of QSOs (defined as in Section 6.2) for a given field by its effective surface. Therefore, the number of quasars per square degree is a quantity insensitive to the instrumental conditions.

In addition, as both in the 1% survey and the main survey, the QSOs can be reobserved several times, we only use the first observation, meaning that we require, respectively, for the 1% and main surveys, `PRIORITY == 103400` and `PRIORITY == 3400`.

7.2. Performance of the Main Selection

First, we estimate the efficiency and purity of the automated QSO catalog, as defined in Section 6.2 for the main selection with nominal exposure time conditions. To achieve this, we coadded the different exposures of the three visually inspected tiles into coadds of ∼1000 s and we apply a posteriori the main selection. Using as the truth, the classification obtained by visually inspecting spectra containing all the coadds, we measure a $99.4\% \pm 0.1\%$ purity and a $93.5\% \pm 0.1\%$ efficiency, for the effective exposure time, corresponding to $T_{\rm eff} \sim 1000$ s. Considering the galaxy contaminant with a good redshift as good tracers of the matter, the purity increases to $99.7\% \pm 0.1\%$. This very high purity of the automated catalog with nominal conditions allows us to use this catalog in the rest of the paper for the validation of the main selection.

Then, we study the performance of the main selection as a function of the effective time, $T_{\rm eff}$. In Figure 14, three different data sets are studied: (1) the three visually inspected tiles, for which we coadded the different exposures in coadds of ∼1000 or ∼4000 s of effective time, (2) the 1% survey with an average of ∼1300 s effective time, and (3) the main survey with an average of ∼1000 s effective time.

The result shown in the top plot of Figure 14 played a crucial role in our choice of the final selection. It clearly shows that the number of quasars has very little dependence on the effective observation time. Whether for $T_{\rm eff} \sim 1000$ s or $T_{\rm eff} \sim 4000$ s, the number of QSOs is ∼200 QSOs and ∼60 QSOs per deg^2 for all QSOs and Lyα forest QSOs, respectively. This stability of the results made it possible to extrapolate the results obtained for the SV ($T_{\rm eff} \sim 4000$ s) to the main survey ($T_{\rm eff} \sim 1000$ s).

The other two plots of Figure 14 again show that the number of QSOs is very stable as a function of $T_{\rm eff}$, even when $T_{\rm eff}$ is below the nominal time, defined for the main survey ($T_{\rm eff} = 1000$ s). By construction, during the main survey, the effective time will suffer from a certain dispersion, $\Delta T_{\rm eff} \sim \pm 150$ s, but the stability of the number of quasars proves that QSO clustering analyses will not have to correct for a possible first-order effect related to the exposure time. Similarly, the excellent uniformity of the number of QSOs as a function of target location over the focal plane, as illustrated by Figure 15, should facilitate clustering analyses.

In conclusion, the performance of the QSO main selection is extremely stable in $T_{\rm eff}$ and uniform as a function of the target location on the focal plane.

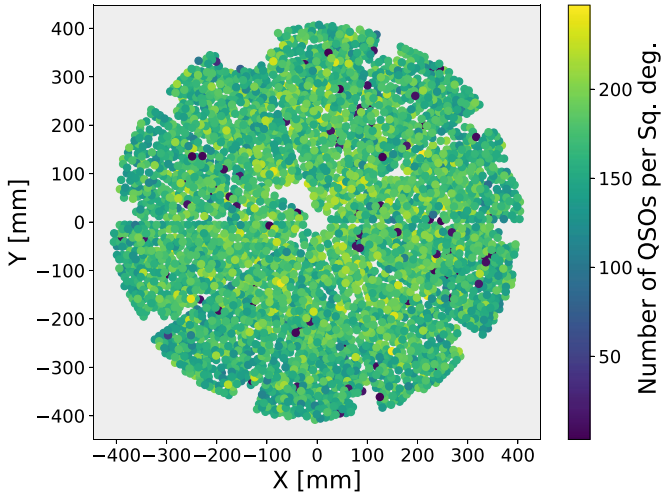

Figure 15. Number of quasars per square degree as a function of the target location on the focal plane. Each petal of the focal plane exhibits a hole at its periphery, corresponding to Guide, Focus, and Alignment (GFA) sensors. One of the 10 petals presents additional holes, due to connection issues with the positioners that were repaired during summer 2021.

7.3. Comparison with SDSS Catalog

As the QSO targets have the highest priority in the DESI fiber assignment, the first 2 months of the main survey already correspond to an effective surface of 1291 deg^2 for the QSO targets. A large fraction of the DESI footprint is covered by the DR16Q SDSS QSO catalog (Lyke et al. 2020). In the DESI main survey, 49,148 QSO targets are also in DR16Q. We use these QSOs as a control sample with which we measure the efficiency (but not the purity because the DR16Q control sample is not complete) defined in Section 6.2. The results shown in Figure 16 are quite similar to those obtained with the visually inspected control sample of QSOs (see Figure 11). The RR algorithm has an efficiency of the order of 90%. The Mg II algorithm allows us to recover low-z QSOs and finally the QN algorithm allows us to achieve a 99% efficiency.

In Figure 17, we compare the redshift measurements of the DESI and DR16Q catalogs. The top left plot shows that the vast majority of QSOs have consistent redshifts. The off-diagonal QSOs (0.8% of the sample) most often correspond to an incorrect association of QSO emission lines, which results in lines that lie off the $z(\mathrm{SDSS}) = z(\mathrm{DESI})$ diagonal.

A visual inspection of one-third of the off-diagonal QSOs that exhibit inconsistent redshifts between the two catalogs is summarized in Figure 18. Only three objects out of 99 show a discrepancy between the visually inspected redshift and the DESI redshift. In contrast, all the SDSS redshifts of the off-diagonal QSOs are inconsistent with the visually inspected redshifts.

The core of the redshift difference distribution, $\delta = z(\mathrm{SDSS}) - z(\mathrm{DESI})$, is shown in the top right plot of Figure 17. It is clearly asymmetric and the mean is significantly different from zero: $\mu(\delta) = (1.1 \pm 0.01) \times 10^{-3}$. The bottom plot of Figure 17 seems to demonstrate that the asymmetry in δ appears only above redshift 2.5, when the Mg II line cannot be used to measure the redshift. A direct comparison of DR16Q redshifts with the systemic redshifts measured with spectra of the reverberation mapping project (Shen et al. 2016) or a more recent publication (Wu & Shen 2022) tend to confirm this discrepancy.

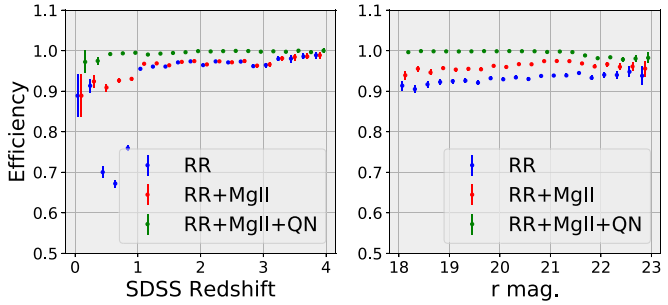

Figure 16. Efficiency as a function of redshift and r mag, using the DR16Q SDSS catalog as a control sample. The efficiency is the fraction of the DR16Q SDSS catalog that is selected in the DESI QSO catalog. The three algorithms, RR, Mg II, and QN are successively applied.

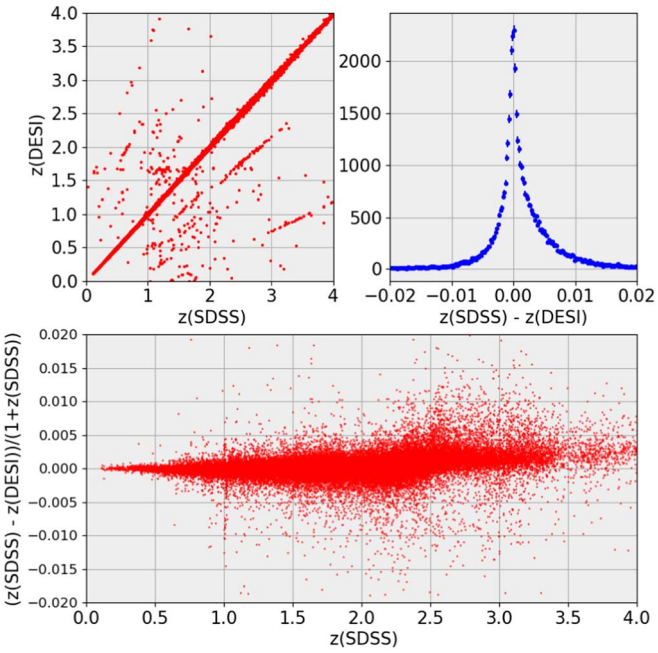

Figure 17. Comparison of DESI redshifts with SDSS redshifts. The objects are matched between the SDSS DR16Q catalog and the QSO catalog for the first 2 months of the DESI main survey.

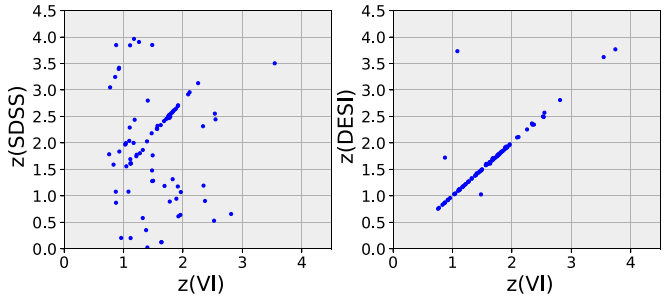

Figure 18. Comparison of the DESI redshifts and the SDSS redshifts with the visually inspected redshifts when the SDSS and DESI redshifts are inconsistent (i.e., for QSOs that lie off the $z(\mathrm{SDSS}) = z(\mathrm{DESI})$ diagonal in the top left plot of Figure 17).

7.4. DESI Redshift Resolution

In the 1% survey, all the QSOs with $z > 1.6$ have been observed at 4 times the nominal exposure time in order to test the infrastructure that will allow DESI to observe the Lyα QSOs 4 times longer that the rest of the QSOs. The 1% survey

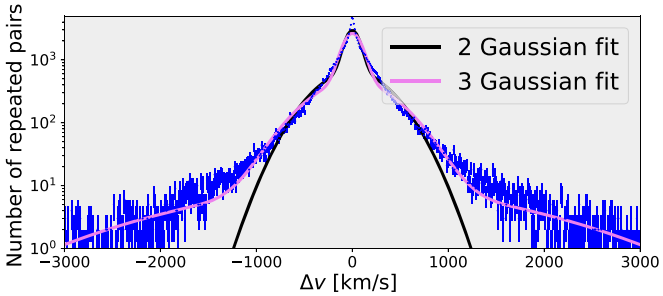

Figure 19. Comparison of the DESI redshifts for several repeats of the same QSO obtained with the 1% survey. The black and violet curves correspond, respectively, to the two-Gaussian and three-Gaussian models.

thus provides several repeats of the same QSO, allowing us to study the DESI redshift resolution. There are 103,350 pairs with $z > 1.6$ that can be used for comparison.

For each pair (i, j) of redshifts, we compute the redshift difference, $\Delta v = (z_i - z_j)/(1 + (z_i + z_j)/2) \times c$ (see Figure 19). The standard deviation of the Δv distribution is $372\,\mathrm{km\,s^{-1}}$, indicating a redshift resolution of the order of $263\,\mathrm{km\,s^{-1}}$. However, Figure 19 shows a non-Gaussian distribution with very wide tails. A two-Gaussian model encounters difficulties in reproducing the tails (black curve). The Δv distribution is better modeled by three Gaussians with $\sigma_1 = 95$, $\sigma_2 = 400$, and $\sigma_3 = 1500\,\mathrm{km\,s^{-1}}$, corresponding to 53%, 44%, and 3%, respectively, of the total distribution.

7.5. Systematics for Automated QSO Catalog

In order to identify the main sources of systematic effects in the QSO target selection, Figure 4 shows the relative QSO target density as a function of each observational parameter. Those plots are obtained for all the QSO targets, including the contaminants, galaxies and stars. It is particularly interesting to reproduce such a figure for the objects retained in the automated QSO catalog. As the purity of this catalog is >99%, all the contaminants were removed.

Figure 20 allows us to compare the systematic effects for the original QSO target catalog (blue curve) and the catalog of QSOs spectroscopically confirmed (red curve) in a part of the South (non-DES) region, observed during the first 2 months of the main survey. This subset of the DESI footprint corresponds to a region, strongly contaminated by stars from the Sgr stream and therefore particularly interesting to study. We observe that all the strong trends in the target densities related to the stellar density in the Galactic plane, or the Sgr stream, vanish in the spectroscopic catalog. Weaker systematic effects are also removed. The methods presented in Chaussidon et al. (2021) should suppress the remaining effects.

7.6. Results

The results in terms of the number of QSOs per square degree are summarized in Table 4. With a 310 $\mathrm{deg^{-2}}$ target density, the main quasar selection selects more than 200 $\mathrm{deg^{-2}}$ quasars, including 60 $\mathrm{deg^{-2}}$ quasars with $z > 2.1$. The QSO densities exceed the project requirements by 20%. We expect a similar gain of 20% in the measurement of the cosmological parameters from clustering of either QSOs or Lyα QSOs compared to the forecasts given in DESI Collaboration et al. (2016a).

We measure a slight difference between the 1% survey and the main survey, on the order of a few percent. This is partly due to the difference in the effective exposure time but mainly due to the regions of the sky observed. These first 2 months of the main survey are located near the Galactic Plane, a region where the imaging is of lower quality, which explains the small observed discrepancy.

The comparison of the distribution of the QSO number as a function of the redshift is remarkably identical for the North and South imaging (see Figure 21). The only area of small discrepancy is at low z, a region where the target selection depends notably on the definition of the stellar morphology ("PSF"). The morphology, which is driven by the z band in the North imaging, is different than in the South imaging where the three optical bands contribute almost equally.

Finally, we compare our results to the density of QSOs as a function of redshift that we can derive from the QLF of Palanque-Delabrouille et al. (2016). In Figure 22, the QLF is corrected for target selection completeness, $\varepsilon(z, r)$, which depends on redshift and r magnitude. This selection completeness is determined from the QSOs in the RF test sample that were not used in the RF training and that pass the selection process described in Section 3. For $r < 22.7$ (blue curve), we obtain an excellent agreement between the prediction from the QLF and the observed number of QSOs. The very small discrepancy observed for $r < 23.0$ (red curve) comes, on the one hand, from uncertainties in the QLF, in particular for faint QSOs, and on the other hand, from the limited number of QSOs available in the RF test sample beyond 22.7 in r.

In conclusion, with a 310 $\mathrm{deg^{-2}}$ target density, the main selection based on an RF approach selects over 200 $\mathrm{deg^{-2}}$ quasars, including 60 $\mathrm{deg^{-2}}$ quasars with $z > 2.1$, exceeding the project requirements by 20%. These QSO densities are in excellent agreement with QLF predictions.

8. Conclusions

In this paper, we present the QSO target selection developed for DESI. It is based on three optical (g, r, z) bands combined with two WISE infrared bands, W1 and W2. QSOs have a stellar morphology, but they are ~2 mag brighter in the near-infrared at all redshifts than stars of similar optical magnitude and color, which provides a powerful method for discriminating against contaminating stars.

During the SV of DESI, we tested several extensions of an initial set of photometric cuts. These included a relaxed definition of stellar morphology and an extension of the r-band magnitude limit. We also developed alternative methods. These included a color cut selection, an RF selection, a selection based on variability in the WISE light curves, and a selection of high-z QSOs based on g-band/r-band dropout techniques.

We first defined a control sample consisting of spectroscopically confirmed QSOs all validated by visual inspection of their spectra. This control sample indicates that the main selection consists of 71% quasars, 16% galaxies, 6% stars, and 5% inconclusive spectra.

In addition, this pure control sample allowed us to develop a method to build an automated QSO catalog from our observations, using three algorithms: the DESI pipeline classifier Redrock, a Mg II broad line finder, and a machine-learning-based classifier QuasarNet. Thanks to our control sample, we estimate that this combined approach achieves a

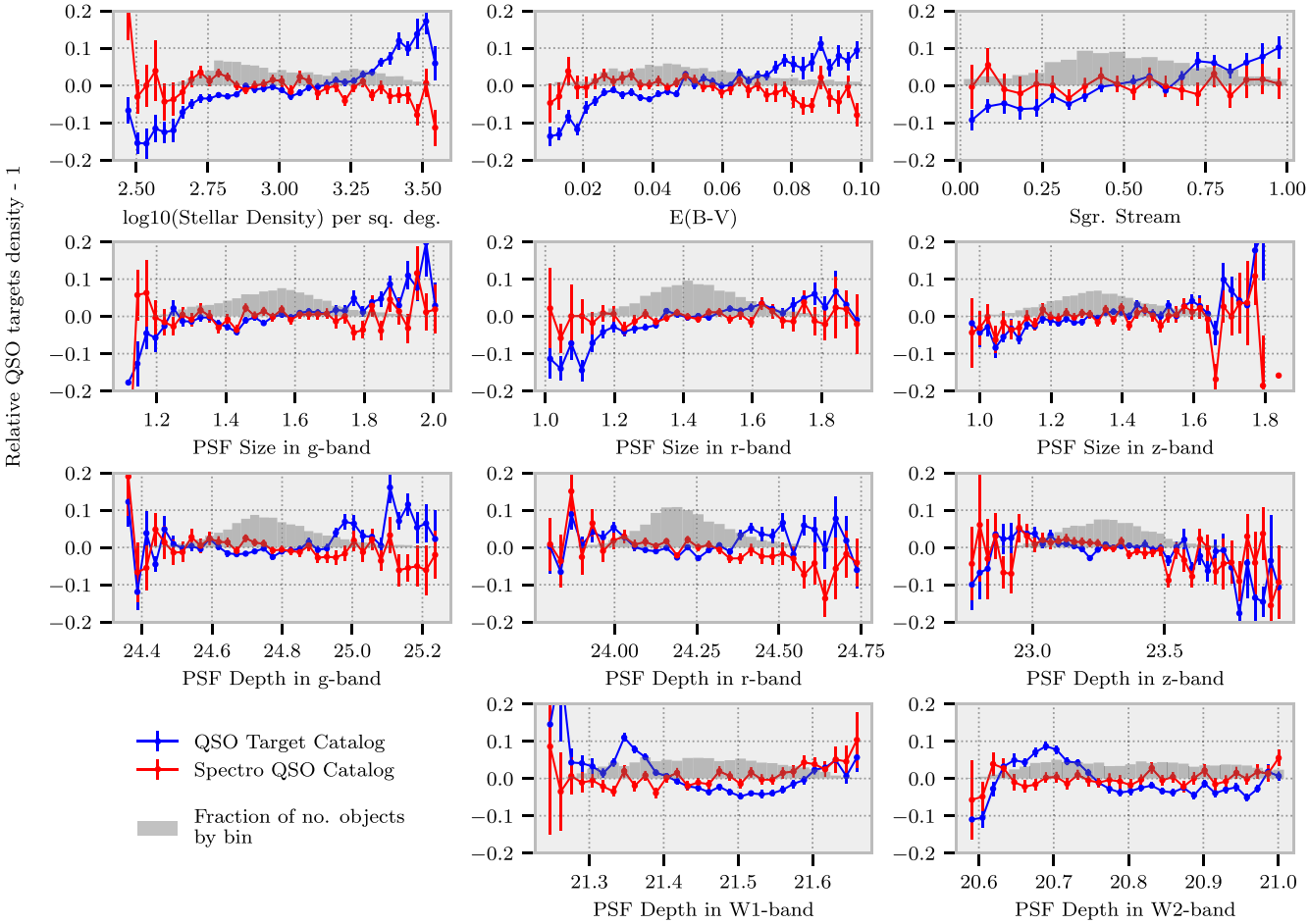

Figure 20. Relative QSO target or QSO densities for a part of the South (non-DES) region as a function of each observational parameter (see Section 4.2.1 for the definition of the parameters). The blue curve represents the density for all the QSO targets while the red curve is obtained for the spectroscopically confirmed QSOs only.

Table 4
Number of QSOs per Square Degree for the 1% and Main Surveys, Obtained with a 310 deg^{-2} Main Selection Target Density

	Number of QSOs (deg^{-2})	Number of Lyα QSOs (deg^{-2})
DESI requirements	170	50
1% survey	211.9 ± 1.2	61.0 ± 0.6
Main survey	205.1 ± 0.4	59.1 ± 0.2

Note. The second and third columns are for all the QSOs and for the $z > 2.1$ QSOs, respectively.

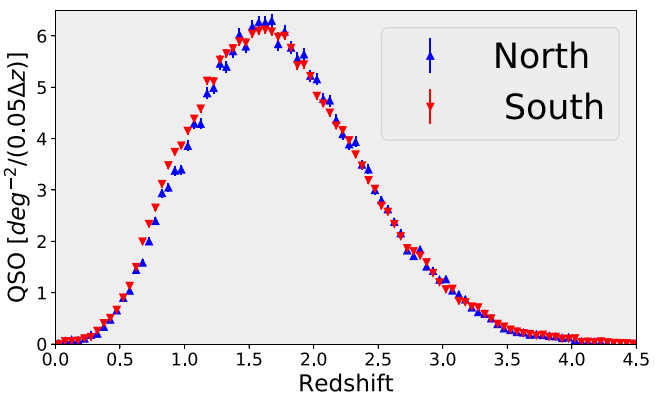

Figure 21. dN/dz for the North and South regions.

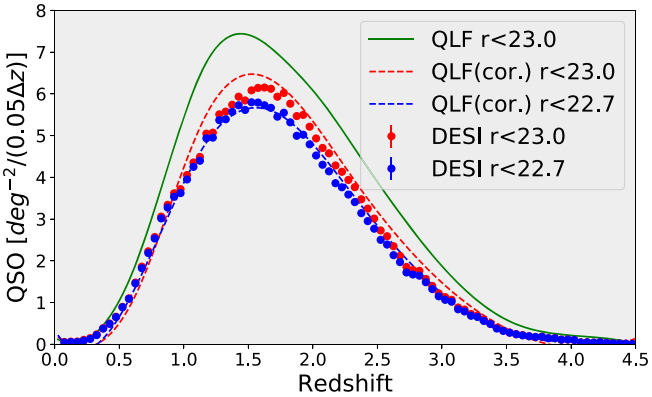

Figure 22. Comparison between QLF predictions and the measured quasar density for $r < 22.7$ and $r < 23.0$. The green curve represents the QLF integrated up to $r = 23.0$. The red and blue curves are computed after correcting by the target selection completeness, $\varepsilon(z, r)$. The blue and red dots correspond to the QSO density obtained with the main survey for $r < 22.7$ and $r < 23.0$ QSO targets, respectively.

99.4% ± 0.1% purity for effective exposure times around the nominal time $T_{\rm eff} \sim 1000$ s

We applied the same approach to analyze the SV fields and to optimize the QSO target selection for the main survey. The optimization was carried out in order to obtain a compromise between the number of targets observed and the number of

confirmed QSOs with an accurate redshift. Our final prescription for the main selection, described in Section 3, is to select $16.5 < r < 23.0$ objects with a stellar morphology ("PSF" in DR9) and with an RF probability greater than a predefined probability threshold, $p_{\rm th}(r)$.

With a 310 deg^{-2} target density, the main survey selection allows DESI to select more than 200 deg^{-2} quasars, including 60 deg^{-2} quasars at redshifts $z > 2.1$, exceeding the project requirements by 20%. The redshift distribution of the confirmed quasars is in excellent agreement with predictions from the QLF of Palanque-Delabrouille et al. (2016).

The first 2 months of the main DESI survey allowed us to collect more than 263,000 QSOs over an effective area of 1291 deg^2. Using this sample, we assess that the redshift distributions of the spectroscopically confirmed QSOs of our selection are almost identical for QSOs selected with North or South imaging. The QSO density is found to be independent of the target location on the focal plane and is not very sensitive to the effective exposure time around the nominal time $T_{\rm eff} \sim 1000$ s.

In addition, the study of QSO target density variations shows strong trends as a function of the stellar density in the Galactic plane or in the Sgr stream. Those effects vanish with the catalog of spectroscopically confirmed QSOs, and the QSO densities as a function of all the other observational parameters remain reasonably flat.

This stability of the QSO density allows us to anticipate that the final QSO catalogs should show low levels of systematic effects. This is an extremely encouraging result for future QSO clustering analyses with DESI data.

This research is supported by the Director, Office of Science, Office of High Energy Physics of the US Department of Energy under contract No. DEAC0205CH11231, and by the National Energy Research Scientific Computing Center, a DOE Office of Science User Facility under the same contract; additional support for DESI is provided by the US National Science Foundation, Division of Astronomical Sciences under contract No. AST-0950945 to the NSF's National Optical-Infrared Astronomy Research Laboratory; the Science and Technologies Facilities Council of the United Kingdom; the Gordon and Betty Moore Foundation; the Heising-Simons Foundation; the French Alternative Energies and Atomic Energy Commission (CEA); the National Council of Science and Technology of Mexico (CONACYT); the Ministry of Science and Innovation of Spain (MICINN), and by the DESI Member Institutions: https://www.desi.lbl.gov/collaborating-institutions.

The DESI Legacy Imaging Surveys consist of three individual and complementary projects: DECaLS, BASS, and MzLS. DECaLS, BASS, and MzLS together include data obtained, respectively, at the Blanco telescope, Cerro Tololo Inter-American Observatory, NSF's NOIRLab; the Bok telescope, Steward Observatory, University of Arizona; and the Mayall telescope, Kitt Peak National Observatory, NOIRLab. NOIRLab is operated by the Association of Universities for Research in Astronomy (AURA) under a cooperative agreement with the National Science Foundation. Pipeline processing and analyses of the data were supported by NOIRLab and the Lawrence Berkeley National Laboratory. Legacy Surveys also uses data products from the Near-Earth Object Wide-field Infrared Survey Explorer (NEOWISE), a project of the Jet Propulsion Laboratory/California Institute of Technology, funded by the National Aeronautics and Space Administration. Legacy Surveys was supported by: the Director, Office of Science, Office of High Energy Physics of the US Department of Energy; the National Energy Research Scientific Computing Center, a DOE Office of Science User Facility; the US National Science Foundation, Division of Astronomical Sciences; the National Astronomical Observatories of China, the Chinese Academy of Sciences and the Chinese National Natural Science Foundation. LBNL is managed by the Regents of the University of California under contract to the US Department of Energy. The complete acknowledgments can be found at https://www.legacysurvey.org/.

The authors are honored to be permitted to conduct scientific research on Iolkam Du'ag (Kitt Peak), a mountain with particular significance to the Tohono O'odham Nation.

A.D.M. was supported by the U.S. Department of Energy, Office of Science, Office of High Energy Physics, under award No. DE-SC0019022. T.W.L. was supported by the Ministry of Science and Technology (MOST 111-2112-M-002-015-MY3), the Ministry of Education, Taiwan (Yushan Young Scholar grant NTU-110VV007), National Taiwan University research grant (NTU-CC-111L894806), and NSF grant AST-1911140.

Data Availability

Data Release 9 of the DESI Legacy Imaging Surveys is available at https://www.legacysurvey.org/dr9/.

The list of QSO targets can be found at https://data.desi.lbl.gov/public/ets/target/catalogs/ and a description of the files is documented in Myers et al. (2022).

All data points used in the published graphs are available at https://doi.org/10.5281/zenodo.6624839.

ORCID iDs

Edmond Chaussidon https://orcid.org/0000-0001-8996-4874
Christophe Yèche https://orcid.org/0000-0001-5146-8533
Nathalie Palanque-Delabrouille https://orcid.org/0000-0003-3188-784X
David M. Alexander https://orcid.org/0000-0002-5896-6313
Jinyi Yang https://orcid.org/0000-0001-5287-4242
Steven Ahlen https://orcid.org/0000-0001-6098-7247
Stephen Bailey https://orcid.org/0000-0003-4162-6619
David Brooks https://orcid.org/0000-0002-8458-5047
Zheng Cai https://orcid.org/0000-0001-8467-6478
Solène Chabanier https://orcid.org/0000-0002-5692-5243
Tamara M. Davis https://orcid.org/0000-0002-4213-8783
Kyle Dawson https://orcid.org/0000-0002-0553-3805
Arjun Dey https://orcid.org/0000-0002-4928-4003
Biprateep Dey https://orcid.org/0000-0002-5665-7912
Daniel J. Eisenstein https://orcid.org/0000-0002-2929-3121
Andreu Font-Ribera https://orcid.org/0000-0002-3033-7312
Enrique Gaztañaga https://orcid.org/0000-0001-9632-0815
Alma X. Gonzalez-Morales https://orcid.org/0000-0003-4089-6924
Julien Guy https://orcid.org/0000-0001-9822-6793
Hiram K. Herrera-Alcantar https://orcid.org/0000-0002-9136-9609
Mustapha Ishak https://orcid.org/0000-0002-6024-466X
Linhua Jiang https://orcid.org/0000-0003-4176-6486
Stephanie Juneau https://orcid.org/0000-0002-0000-2394
Robert Kehoe https://orcid.org/0000-0002-7101-697X
Theodore Kisner https://orcid.org/0000-0003-3510-7134
Andras Kovács https://orcid.org/0000-0002-5825-579X

Anthony Kremin https://orcid.org/0000-0001-6356-7424
Ting-Wen Lan https://orcid.org/0000-0001-8857-7020
Martin Landriau https://orcid.org/0000-0003-1838-8528
Laurent Le Guillou https://orcid.org/0000-0001-7178-8868
Michael E. Levi https://orcid.org/0000-0003-1887-1018
Paul Martini https://orcid.org/0000-0002-4279-4182
Aaron M. Meisner https://orcid.org/0000-0002-1125-7384
John Moustakas https://orcid.org/0000-0002-2733-4559
Jeffrey A. Newman https://orcid.org/0000-0001-8684-2222
Jundan Nie https://orcid.org/0000-0001-6590-8122
Will J. Percival https://orcid.org/0000-0002-0644-5727
Francisco Prada https://orcid.org/0000-0001-7145-8674
Anand Raichoor https://orcid.org/0000-0001-5999-7923
Edward Schlafly https://orcid.org/0000-0002-3569-7421
David Schlegel https://orcid.org/0000-0002-5042-5088
Ting Tan https://orcid.org/0000-0001-8289-1481
Gregory Tarlé https://orcid.org/0000-0003-1704-0781
Rongpu Zhou https://orcid.org/0000-0001-5381-4372
Zhimin Zhou https://orcid.org/0000-0002-4135-0977
Hu Zou https://orcid.org/0000-0002-6684-3997

References

Abareshi, B., Aguilar, J., Ahlen, S., et al. 2022, AJ, 164, 207
Alam, S., Aubert, M., Avila, S., et al. 2021, PhRvD, 103, 083533
Alexander, D. M., Davis, T. M., Chaussidon, E., et al. 2022, arXiv:2208.08517
Allende Prieto, C., Cooper, A. P., Dey, A., et al. 2020, RNAAS, 4, 188
Antoja, T., Ramos, P., Mateu, C., et al. 2020, A&A, 635, L3
Busca, N., & Balland, C. 2018, arXiv:1808.09955
Busca, N. G., Delubac, T., Rich, J., et al. 2013, A&A, 552, A96
Chabanier, S., Palanque-Delabrouille, N., Yèche, C., et al. 2019, JCAP, 2019, 017
Chambers, K. C., Magnier, E. A., Metcalfe, N., et al. 2016, arXiv:1612.05560
Chaussidon, E., Yèche, C., Palanque-Delabrouille, N., et al. 2021, MNRAS, 509, 3904
Cooper, A. P., Koposov, S. E., Allende Prieto, C., et al. 2022, arXiv:2208.08514
Croom, S. M., Smith, R. J., Boyle, B. J., et al. 2001, MNRAS, 322, L29
Cutri, R. M., Wright, E. L., Conrow, T., et al. 2021, VizieR Online Data Catalog, II/328
Dawson, K. S., Kneib, J.-P., Percival, W. J., et al. 2016, AJ, 151, 44
Dawson, K. S., Schlegel, D. J., Ahn, C. P., et al. 2013, AJ, 145, 10
DESI Collaboration, Aghamousa, A., Aguilar, J., et al. 2016a, arXiv:1611.00036
DESI Collaboration, Aghamousa, A., Aguilar, J., et al. 2016b, arXiv:1611.00037
Dey, A., Schlegel, D. J., Lang, D., et al. 2019, AJ, 157, 168
Donley, J. L., Koekemoer, A. M., Brusa, M., et al. 2012, ApJ, 748, 142
du Mas des Bourboux, H., Rich, J., Font-Ribera, A., et al. 2020, ApJ, 901, 153
Eisenstein, D. J., Weinberg, D. H., Agol, E., et al. 2011, AJ, 142, 72
Farr, J., Font-Ribera, A., & Pontzen, A. 2020, JCAP, 2020, 015
Gaia Collaboration, Brown, A. G. A., Vallenari, A., et al. 2018, A&A, 616, A1
Hahn, C., Wilson, M. J., Ruiz-Macias, O., et al. 2022, arXiv:2208.08512
Hou, J., Sánchez, A. G., Ross, A. J., et al. 2021, MNRAS, 500, 1201
Lan, T.-W., Tojeiro, R., Armengaud, E., et al. 2023, ApJ, 943, 68
Lang, D., Hogg, D. W., & Mykytyn, D. 2016, The Tractor: Probabilistic astronomical source detection and measurement, Astrophysics Source Code Library, ascl:1604.008
Levi, M., Bebek, C., Beers, T., et al. 2013, arXiv:1308.0847
Lyke, B. W., Higley, A. N., McLane, J. N., et al. 2020, ApJS, 250, 8
McDonald, P. 2003, ApJ, 585, 34
McGreer, I. D., Jiang, L., Fan, X., et al. 2013, ApJ, 768, 105
Meisner, A. M., Lang, D., & Schlegel, D. J. 2017, AJ, 154, 161
Myers, A. D., Moustakas, J., Bailey, S., et al. 2023, AJ, 165, 50
Myers, A. D., Palanque-Delabrouille, N., Prakash, A., et al. 2015, ApJS, 221, 27
Neveux, R., Burtin, E., de Mattia, A., et al. 2020, MNRAS, 499, 210
Palanque-Delabrouille, N., Magneville, C., Yeche, C., et al. 2016, A&A, 587, A41
Palanque-Delabrouille, N., Yeche, C., Myers, A. D., et al. 2011, A&A, 530, A122
Powers, D. 2011, J. Mach. Learn. Technol., 2, 37
Raichoor, A., Eisenstein, D. J., Karim, T., et al. 2020, RNAAS, 4, 180
Raichoor, A., Moustakas, J., Newman, J. A., et al. 2022, arXiv:2208.08513
Richards, G. T., Fan, X., Newberg, H. J., et al. 2002, AJ, 123, 2945
Ross, N. P., Myers, A. D., Sheldon, E. S., et al. 2012, ApJS, 199, 3
Ruiz-Macias, O., Zarrouk, P., Cole, S., et al. 2020, RNAAS, 4, 187
Schlafly, E. F., & Finkbeiner, D. P. 2011, ApJ, 737, 103
Schlegel, D. J., Finkbeiner, D. P., & Davis, M. 1998, ApJ, 500, 525
Shen, Y., Brandt, W. N., Richards, G. T., et al. 2016, ApJ, 831, 7
Slosar, A., Iršič, V., Kirkby, D., et al. 2013, JCAP, 2013, 026
Stern, D., Eisenhardt, P., Gorjian, V., et al. 2005, ApJ, 631, 163
Wang, F., Wu, X.-B., Fan, X., et al. 2016, ApJ, 819, 24
Wright, E. L., Eisenhardt, P. R. M., Mainzer, A. K., et al. 2010, AJ, 140, 1868
Wu, Q., & Shen, Y. 2022, ApJS, 263, 42
Yang, J., Fan, X., Wu, X.-B., et al. 2017, AJ, 153, 184
Yèche, C., Palanque-Delabrouille, N., Claveau, C.-A., et al. 2020, RNAAS, 4, 179
Yeche, C., Petitjean, P., Rich, J., et al. 2010, A&A, 523, A14
York, D. G., Adelman, J., Anderson, J. E., Jr., et al. 2000, AJ, 120, 1579
Zarrouk, P., Burtin, E., Gil-Marín, H., et al. 2018, MNRAS, 477, 1639
Zhou, R., Dey, B., Newman, J. A., et al. 2023, AJ, 165, 58
Zhou, R., Newman, J. A., Dawson, K. S., et al. 2020, RNAAS, 4, 181
Zou, H., Zhou, X., Fan, X., et al. 2017, PASP, 129, 064101